# Quantum Well Intersubband Transition Detection and Modulation

Thesis by

Yuanjian Xu

In Partial Fulfillment of the Requirements
for the Degree of
Doctor of Philosophy

California Institute of Technology
Pasadena, California

1997

(Defended October 24, 1996)

# Acknowledgments

First of all, I would like to thank my advisor, Professor Amnon Yariv, for giving me the opportunity and support of studying and doing research in his group. I appreciate the freedom of pursuing research projects in his group and his constant guidance. I have enjoyed interacting with the many talented students in the group. In particular, I'd like to thank Dr. Ali Shakouri for his very generous help. The fruitful discussions with Dr. Gilad Almogy were appreciated.

I would also like to thank Dr. T. R. Chen, who was my previous advisor when I was a graduate student at University of Electronic Science and Technology of China, for introducing me into Prof. Yariv's group and for his various help. I'd like to thank his wife, Yuhua Zhuang, for teaching me liquid phase epitaxy growth and the basic semiconductor processing scheme.

I benefited from many of the students previously and currently in the group, namely, Dr. Randal A. Salvatore, Dr. John O'Brien, Xiaolin Tong, Dr. John Kitching, Dr. Tony Kewitsch, Dr. John Iannelli, Andrew Tong, Matt McAdams, Dr. Joseph Rosen, Dr. Sergei Orlov, Bill Marshall, Doruk Engin, Jing Feng, Reginald Lee, and Dan Provenzano. Thanks also go to Reginald Lee and Dan Provanzano for their in-depth proofreading of this thesis.

It was a very pleasant experience working with Prof. Axel Scherer's students (Weihua Xu, Chuang-chan Chen, Oskar Painter, and Joyce Wong). I appreciate their help. I especially would like to thank Prof. Scherer for his trust in me and his many fruitful suggestions.

I owe thanks to Prof. David Rutledge and his students for letting me use their wire bonder (wire bonding is the last step to success). Almost all the wire bonding work was done using their bonder. Specifically, I'd like to thank Shijie Li, Alina Moussessian, Dr. Mike DeLisio, and Dr. Victor Lubecke.

I appreciated suggestions from Dr. Timothy N. Krabach at JPL in the early stage of the detector work.

I want to thank the Caltech staff members, Jana Mercado, Kevin Cooper, and Ali Ghaffari, for their help in getting things running.

Finally, I would like to thank my parents and my wife for their love, encouragement, and support.

# Abstract

This thesis is a theoretical and experimental investigation of the intersubband transitions in quantum well structures. The I-V characteristics, infrared absorption spectra, and photoresponse spectra of superlattices are used to characterize multiple quantum well structure properties in unipolar devices.

An important numerical method for solving the problem of bound-to-continuum transitions, the transfer matrix method, is presented for the self-consistent calculations. Although the boundary conditions are relaxed due to the calculation self-consistentcy, inappropriate boundary conditions were previously included in the literature.

The first observation of the quantum interference effect in the photocurrent spectra is described using a weakly coupled bound-to-continuum transition quantum well structure and electric field domain formation in the device. This effect persists even at high biases where Kronig-Penny minibands of periodic superlattice potential in the continuum are destroyed. Using this observation, the electric field domain formation and the electron coherence length in superlattices were analyzed. A large off-resonant energy level alignment between two neighboring wells in the high field domain was observed. The effect of temperature on the transport properties was also discussed. As a further study of electric field domain formation in superlattices, an optical experiment using Stark effect is suggested.

The dependence of the absorption spectral linewidth of quantum well intersubband transitions on the electron population in the well is experimentally demonstrated using field-induced charge transfer and thermal-induced charge transfer in an asymmetric coupled quantum well structure. We show that this population-induced broadening is very important in the broadening of intersubband transitions in quantum well structures and that previously reported linewidth values for the contribution from donor scattering were overestimated. Many body effects and single-particle band non-parabolicity are the likely causes. An electronic light chopper based on population modulation was fabricated using the asymmetric coupled quantum well structure. A modulation depth of 45% has been demonstrated using 50 periods of the coupled well structure.

# Contents

# List of Figures

# Chapter 1

# Introduction

Semiconductor quantum well structures have been of great interest for both practical applications and academic interests. Using these structures, we can engineer the band structure so as to possess desired optical emission or absorption involving both conduction band and valence band (the interband transitions), or involving subbands in quantum well structures within only conduction band or only valence band (the intersubband transitions). In interband detectors, electrons in the valence band are photo-excited to the conduction band and the photo-excited carriers, in the presence of an applied field, are collected and they contribute to photocurrent. A detector of this type can detect photons with energy larger than the material energy gap. By controlling the material energy gap, the absorption spectrum and hence the photoresponse spectrum of the detector can be changed. The detection of radiation at around 10 $\mu$m wavelength will require a material with small energy gap of about 100 meV when interband transitions are used. In practice, it is difficult to fabricate devices with very small energy gap materials. Quantum well structures can provide intersubband transitions for the long wavelength infrared radiation detection. In addition, intersubband transition energies can be modified by designing the quantum well parameters, adding extra freedom to the design of semiconductor devices.

Intersubband transitions have been studied by many researchers. Esaki and Sakaki [1] first suggested using GaAs/AlGaAs multiple quantum wells (MQWs) to obtain large intersubband transition optical absorption. In 1983, Smith et al. [2] and Chiu et al. [3] first demonstrated experimentally intersubband and bound-to-continuum infrared detectors, while Gurnick and DeTemple [4] discussed theoretically, enhancement of intersubband transition optical nonlinearities. In 1985, West and Eglash [5] demonstrated intersubband absorption at a wavelength of 10 $\mu$m with large oscillator strength of the transition. Following these results, researchers now have a relatively detailed understanding of intersubband absorption selection rules, oscillator strength, intersubband transition energy spacings including many-body effects, absorption line shapes.

One of the applications of intersubband transitions is their use in infrared photodetectors. Among the materials used for intersubband studies, GaAs/AlGaAs has been widely used because of the mature crystal growth and processing technologies. Currently, highly uniform, large area, cost effective, high sensitivity focal plane detector arrays can be achieved [6]. In addition, the current GaAs technology allows the monolithic integration of quantum well infrared detectors with high-speed GaAs multiplexer and other electronics.

For infrared camera applications, large focal plane arrays with moderate sensitivity and low cost are required. PtSi Schottky barrier detector arrays have been studied for mid-wavelength infrared (MWIR) (3 to 5 $\mu$m) applications [7]. IrSi Schottky barrier detectors [8] and SiGe heterojunction internal photoemission detectors [9] have been developed for long-wavelength infrared (LWIR) (7.5 to 12 $\mu$m) applications, but they have large dark currents. GaAs/AlGaAs quantum well infrared photodetectors are good candidates for LWIR spectral range.

## 1.1 Thesis outline

The work described in this thesis concentrates mainly on the applications of the quantum well intersubband transitions for infrared light detection and modulation based on the GaAs/AlGaAs material system. It is possible to design different intersubband transition energies because of the freedom to choose the quantum well parameters. For photodetector applications, however, the range of tuning the intersubband transition energies for given quantum well material is narrow and is discussed in Chapter 2. The intersubband transition absorption, detector photoresponse, and dark current are also described.

It is important to include many body effects in considering intersubband transition energies at high doping densities. It is thus necessary to perform numerical calculations self-consistently. Chapter 3 presents the transfer matrix method for solving one-dimensional differential equations. Although other numerical methods might have some advantages for certain applications, the transfer matrix method is very useful for bound-to-continuum transition calculations.

In the discussion of electric field domain formation, the electron coherence length is an important parameter. Chapter 4 describes the first observation of the quantum interference effect in the photocurrent spectra of a weakly coupled bound-to-continuum multiple quantum well structure. The electron coherence length in the superlattice was also estimated, and the observation was used to investigate electric field domain formation induced by sequential resonant tunneling. Finally, the effect of temperature on the transport properties was also analyzed.

The last chapter is devoted to a discussion of experimental measurement of the intersubband transition population-induced broadening. It will be shown that the population-induced broadening has a significant contribution to the absorption linewidth. The linewidth caused by donor scattering was previously over-estimated in the literature. The electrically induced population change in a selectively doped asymmetric double quantum well structure was used in the design of infrared modulators monolithically integrated with a photodetector.

# References

[1] L. Esaki and H. Sakaki, "New photodetector," IBM Tech. Disc. Bull., vol. 20, no. 6, pp. 2456-2457, 1977.

[2] J. S. Smith, L. C. Chiu, S. Margalit, A. Yariv, A. Y. Cho, "A new infrared detector using electron-emission from multiple quantum wells," J. Vac. Sci. Technol. B, vol. 2, no. 2, pp. 376-378, 1983.

[3] L. C. Chiu, J. S. Smith, S. Margalit, A. Yariv, A. Y. Cho, "Application of internal photoemission from quantum well and heterojunction superlattices to infrared photodetectors," Infrared Phys., vol. 23, no. 2, pp. 93-97, 1983.

[4] M. K. Gurnick, T. A. Detemple, "Synthetic non-linear semiconductors," IEEE J. Quantum Electron., vol. 19, no. 5, pp. 791-794, 1983.

[5] L. C. West and S. J. Eglash, "First observation of an extremely large-dipole infrared transition within the conduction band of a GaAs quantum well," Appl. Phys. Lett., vol. 46, no. 12, pp. 1156-1158, 1985.

[6] L. J. Kozlowski, G. M. Williams, R. E. DeWames, J. W. Stayt, Jr., V. Swami-

nathan, K. G. Glogovsky, R. E. Leibenguth, L. E. Smith, and W. A. Gault, "128 x 128 GaAs/AlGaAs QWIP infrared focal plane array with background limited sensitivity at 40K," submitted for publication.

[7] T. S. Villani, W. F. Kosonocky, F. V. Shallcross, J. V. Groppe, G. M. Meray, J. J. O'Neill, III, and B. J. Esposito, "Construction and performance of a 320 x 244-element IR-CCD imager with PtSi SBDs," SPIE, vol. 1107, pp. 9-21, 1989.

[8] B. Y. Tsaur, M. M. Weeks, R. Trubiana, P. W. Pellegrini, and T. R. Yew, "IrSi Schottky-barrier infrared detectors with 10 $\mu$m cutoff wavelength," IEEE Electron Device Lett., vol. 9, no. 12, pp. 650-653, 1988.

[9] T. L. Lin and J. Maserjian, "Novel $\mathrm{Si}_{1-x}\mathrm{Ge}_x$/Si heterojunction internal photoemission long-wavelength infrared detectors," Appl. Phys. Lett., vol. 57, no. 14, pp. 1422-1424, 1990.

# Chapter 2

# Quantum states and quantum well intersubband infrared photodetectors

In this chapter, electronic subbands, intersubband transition rates, selection rules and oscillator strength sum rule will be described. When a simple quantum well structure is used in a detector application, the intersubband transition energy can be tuned over a small range by changing the well width if the barrier height is fixed. A large transition energy tuning range can be realized by changing the barrier height. Two main parameters in detector characterization, photoresponse and dark current, will be reviewed and discussed. In bound-to-continuum MQW structures, the normalized dark current ($I_d/T$) was shown to have an exponential dependence on the inverse temperature over several orders of magnitude change of current. This indicates the domination of dark current by thermionic emission process for temperature above ~80 K.

## 2.1 Electronic subbands

When a thin narrow energy gap material is sandwiched between wide energy gap ones, the carrier motion normal to the layers is quantized and a sequence of electronic subbands is formed. In the envelope function approximation, the spatial dependence of the electron wavefunction in the conduction band, as an example, is written as

$$\Phi(\mathbf{r}) = \psi(z)e^{i\mathbf{k}_{//}\cdot\mathbf{r}_{//}}u_c(\mathbf{r}), \tag{2.1}$$

where $\psi(z)$ is the slowly varying envelope function, $u_c(\mathbf{r})$ is the Bloch function periodic with the crystal lattices, and $\mathbf{k}_{//}$ is the in-plane wave vector. It is also assumed that the Bloch functions are the same for different materials constituting the heterostructures. From the Ben Daniel-Duke model, the envelope functions are solutions to the Schrödinger equation [1]:

$$-\frac{\hbar^2}{2}\frac{d}{dz}\left(\frac{1}{m^*(z)}\frac{d}{dz}\right)\psi_i(z) + \frac{\hbar^2 k_{//}^2}{2m^*(z)}\psi_i(z) + V(z)\psi_i(z) = E_i\psi_i(z), \tag{2.2}$$

where $\hbar$ is the Plank constant, $m^*(z)$ is the position dependent effective mass of the electron, $E_i$ is the $i^{th}$ quantized energy level, $\psi_i$ is the corresponding envelope function, and $V(z)$ is the potential distribution. The second term on the left-hand side of the above equation is zero at the subband edge ($k_{//} = 0$). The integration of

Equation (2.2) across a heterostructure boundary will require that

$$\psi_i(z) \text{ and } \frac{1}{m^*(z)}\frac{d\psi_i}{dz} \tag{2.3}$$

be continuous across the interface.

In a single quantum well case as shown in Figure 2.1, if we assume piecewise constant potentials for the well and the barriers (the potential $V(z)$ is $V_w$ for the well, and $V_{b1}, V_{b2}$ for the two barriers, respectively), the bound state subband energies satisfy the following equation

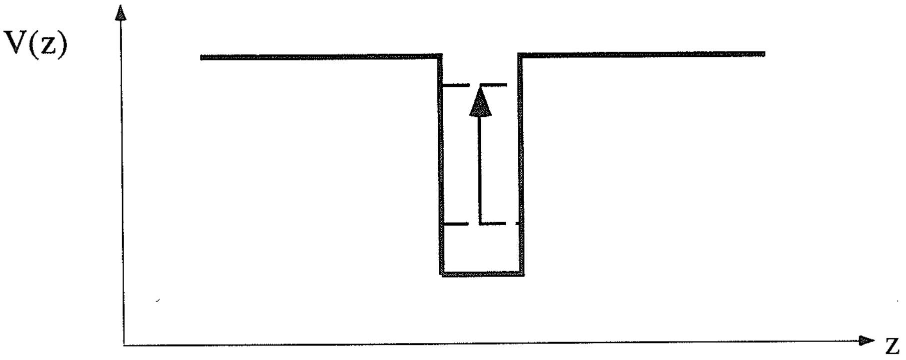

Figure 2.1: Single quantum well with two bound states.

$$\tan(k_w d) = \frac{\frac{k_w}{m_w^*}\left(\frac{k_{b1}}{m_{b1}^*} + \frac{k_{b2}}{m_{b2}^*}\right)}{\left(\frac{k_w}{m_w^*}\right)^2 - \frac{k_{b1}}{m_{b1}^*}\frac{k_{b2}}{m_{b2}^*}}, \tag{2.4}$$

where $k_{b1,b2} = \frac{\sqrt{2m_{b1,b2}^*(V_{b1,b2}-E)}}{\hbar}$, $k_w = \frac{\sqrt{2m_w^*(E-V_w)}}{\hbar}$, $d$ is the well thickness, $E$ is the bound state energy.

Figure 2.2 shows the theoretical intersubband transition energy as a function of well width for a simple quantum well structure suitable for making detectors in the wavelength range of $3 \sim 15\mu$m using a GaAs well and direct energy gap $\mathrm{Al}_x\mathrm{Ga}_{1-x}\mathrm{As}$ ($x < 0.45$) as barrier material. In the calculation, the intersubband transition energy is taken to be the cutoff transition energy ($V_b - E_0$) in the case of bound-to-continuum transition (where there is only one bound state in the well); the transition energy is $E_1 - E_0$ for bound-to-bound transition (where there are two bound states in the well) with $E_1$ close to the barrier. More bound states in the well are not considered for this simple structure because the transition dipole matrix element (which is defined in the next section) is much smaller between the ground state and higher order bound states. The well width can not be very large because the photo-excited electron has a small probability of tunneling out of the well when the excited state is deep in the well, which is undesirable for detector applications. For fixed barrier height, the transition energy can be tuned over a small range by changing the well width. When the barrier height is low (or x is small), the transition energy changes by about 10 meV over a relatively large well width range. The tuning range for larger barrier heights is, however, much larger, which implies that the transition energy is more sensitive to well width fluctuation in this case.

In the calculation of the energy levels in highly doped quantum well structures, it is important to use the Hartree approximation and include many body effects. This will be discussed in the next chapter.

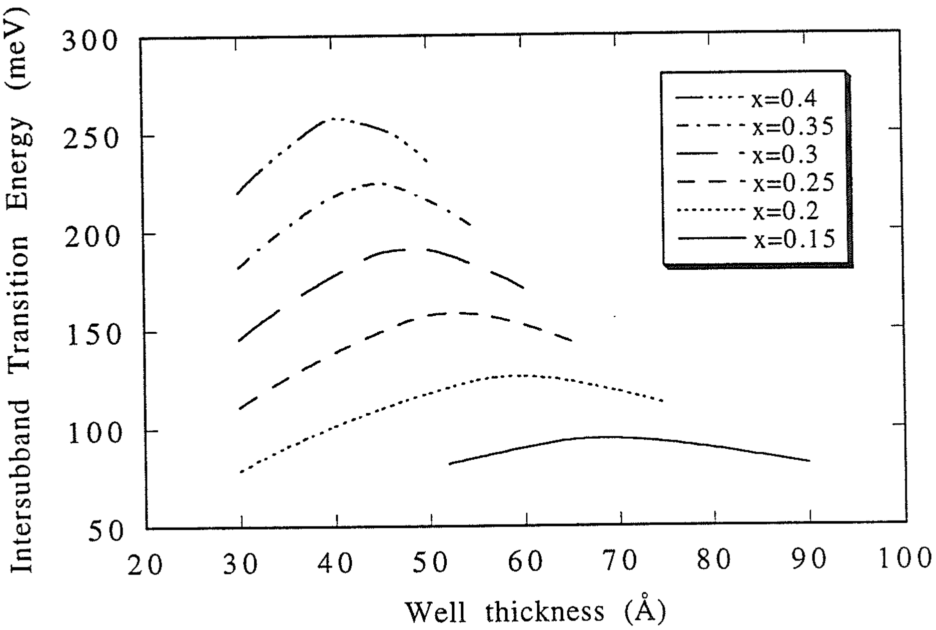

Figure 2.2: Theoretical intersubband transition energy versus GaAs well width for different Al concentrations in the barriers of single quantum well structures.

## 2.2 Intersubband transition selection rule and sum rule

The interaction of an electron in a quantum well structure with an electromagnetic field is calculated using perturbation theory. The interaction Hamiltonian responsible for optical transitions is given by [2]

$$H' = -\frac{e}{m}\mathbf{A}(r) \cdot \mathbf{p}, \tag{2.5}$$

where $\mathbf{A}$(r) is the vector potential of the electromagnetic field, $\mathbf{p}$ is the electron momentum operator. The optical matrix element for a transition between two subbands is proportional to

$$\begin{aligned} &< \Phi_j|\mathbf{A}(r) \cdot \mathbf{p}|\Phi_i >\approx \\ &\textstyle\int_V d^3r u_j^*(r)(\hat{\epsilon} \cdot \mathbf{p})u_i(r)A_0 \int_V d^3r f_j^*(r) f_i(r) + \\ &\textstyle\int_V d^3r u_j^*(r)u_i(r)A_0 \int_V d^3r f_j^*(r)(\hat{\epsilon} \cdot \mathbf{p}) f_i(r), \end{aligned} \tag{2.6}$$

where electronic wavefunction $\Phi_{i(j)} = f_{i(j)}(r)u_{i(j)}(r)$, $f_{i(j)}$ is the envelope function for the initial state (the final state), $u_{i(j)}(r)$ are the Bloch functions, and $\hat{\epsilon}$ is the optical field polarization vector. We have used the rapid spatial oscillation of the Bloch function to separate the integral. From the orthogonality and normalization relations of the Bloch functions, the above equation becomes

$$\begin{aligned} &< \Phi_j|\mathbf{A}(r) \cdot \mathbf{p}|\Phi_i > \\ &\approx< u_j|\hat{\epsilon} \cdot \mathbf{p}|u_i > A_0 \textstyle\int_V d^3r f_j^*(r) f_i(r) + \delta_{i,j} A_0 < f_j|\hat{\epsilon} \cdot \mathbf{p}|f_i > . \end{aligned} \tag{2.7}$$

For intersubband transitions, the initial state and final state are in the same band and have the same Bloch functions. Thus, the first term on the right-hand side of Equation

(2.7) is zero. The second term is responsible for the intersubband transitions. Let $f_i = \frac{1}{\sqrt{s}}\psi_i(z)e^{i\mathbf{k}_{//,i}\cdot\mathbf{r}_{//}}$,

$$\begin{aligned} &< f_j|\hat{\epsilon}\cdot\mathbf{p}|f_i > \\ &= (\epsilon_x\hbar k_x + \epsilon_y\hbar k_y)\delta_{\mathbf{k}_{//,i},\mathbf{k}_{//,j}}\delta_{ij} + \epsilon_z < \psi_j|p_z|\psi_i > \delta_{\mathbf{k}_{//,i},\mathbf{k}_{//,j}}. \end{aligned} \tag{2.8}$$

The polarizations $\epsilon_x$, $\epsilon_y$ give rise to allowed transtions only if the initial and final states coincide. The intrasubband absorption (i=j) cannot be reasonably treated in the static limit without including scattering mechanisms. One can see that only the polarization $\epsilon_z$ term on the right hand side of Equation (2.8) contributes to the intersubband transitions. This equation implies that the optical matrix element is non-zero only when the optical field has non-zero polarization component along the crystal growth direction, provided that the in-plane wavevector of the carrier is conserved (vertical transitions in the $\mathbf{k}_{//}$ space). Thus, a 45° edge mirror, or a grating [4] is often used to couple the infrared light into a quantum well structure. In addition, if the hetersotructure Hamiltonian has a definite parity the initial and final subbands should be of opposite parities.

The oscillator strength for a transition from the $i^{th}$ subband to the $j^{th}$ subband is defined as

$$f_{ij} = \frac{2m^*}{\hbar^2}(E_j - E_i)|\mu_{ij}|^2, \tag{2.9}$$

where $\mu_{ij} = (\hat{\epsilon}\cdot\hat{e}_z) < \psi_j|z|\psi_i >$. From the commutator of the $z$ and $p_z$ operators, it can be shown that the summation of the oscillator strength over all the final states is unity, that is,

$$\sum_j f_{ij} = 1, \tag{2.10}$$

where the dependence of $m^*$ on the position and the band nonparabolicity are neglected. Reference [3] gives detailed discussion of the oscillator strength sum rule including the effects of band nonparabolicity. Checking the oscillator strength sum rule in numerical calculations is important, especially for the calculation of bound-to-continuum transitions, where the quantum well structure is placed in a large box.

## 2.3 Intersubband absorption

Once the dipole matrix element is calculated, we could calculate the intersubband transition rate and the absorption. From Fermi's golden rule, the transition rate from the $i^{th}$ state to the $j^{th}$ state is

$$\Gamma_{ij} = \frac{2\pi}{\hbar} | < \Phi_j | H' | \Phi_i > |^2 \delta(E_j - E_i - \hbar\omega), \tag{2.11}$$

The absorption is given by

$$\alpha(\hbar\omega) = \hbar\omega \frac{\Gamma_{ij}}{I} N_{2D}, \tag{2.12}$$

where $I$ is the incident light intensity, $N_{2D}$ is the $i^{th}$ subband two-dimensional population, and the excited state is assumed to be empty. If we use Lorentzian lineshape function, the above equation can be expressed as

$$\alpha(\hbar\omega) = \frac{\pi q^2}{\hbar n c \epsilon_0} N_{2D} |\mu_{ij}|^2 \hbar\omega \frac{\hbar / T_2}{(E_j - E_i - \hbar\omega)^2 + (\hbar / T_2)^2}, \tag{2.13}$$

where $n$ is the refractive index, $c$ is the speed of light in vacuum, $\epsilon_0$ is the vacuum permittivity, and $T_2$ is the transition dephasing time.

Figure 2.3 shows the calculated absorption spectrum for a structure with $Al_{0.21}Ga_{0.79}As$ barriers and (a) 62 Å, (b) 58 Å, and (c) 56 Å GaAs wells. As the well gets narrower, the contribution from the continuum states becomes larger because of the oscillator strength sum rule. The stronger absorption for bound-to-bound transition, compared with that for bound-to-continuum transition, is due to the fact that the wavefunction of the excited bound state is more localized and that the dipole matrix element involves overlap integral of the initial and final state wavefunctions. The absorption peak shifts very slightly because it is still dominated by the bound-to-bound transition.

When the well size is further reduced, there will be only one bound state in the well. A natural question one can ask is what would be the absorption peak position ($E_{peak}$). There are three possibilities for the location of the absorption peak, (1) the cutoff transition energy; (2) $k_z d = m\pi$, where $k_z$ is the wave vector in the well and m is a positive integer; (3) the transition from the bound state to the state in the continuum with the largest oscillator strength (which we will call the resonance state). The first two possibilities give decreasing $E_{peak}$ when the well size is decreased. It has been experimentally shown that the absorption peak corresponds to the transition from the bound state to the resonance state in the continuum [5]. An example is shown in Figure 2.4. It can be seen that the bound-to-continuum transition energy is not a monotonic function of the well width.

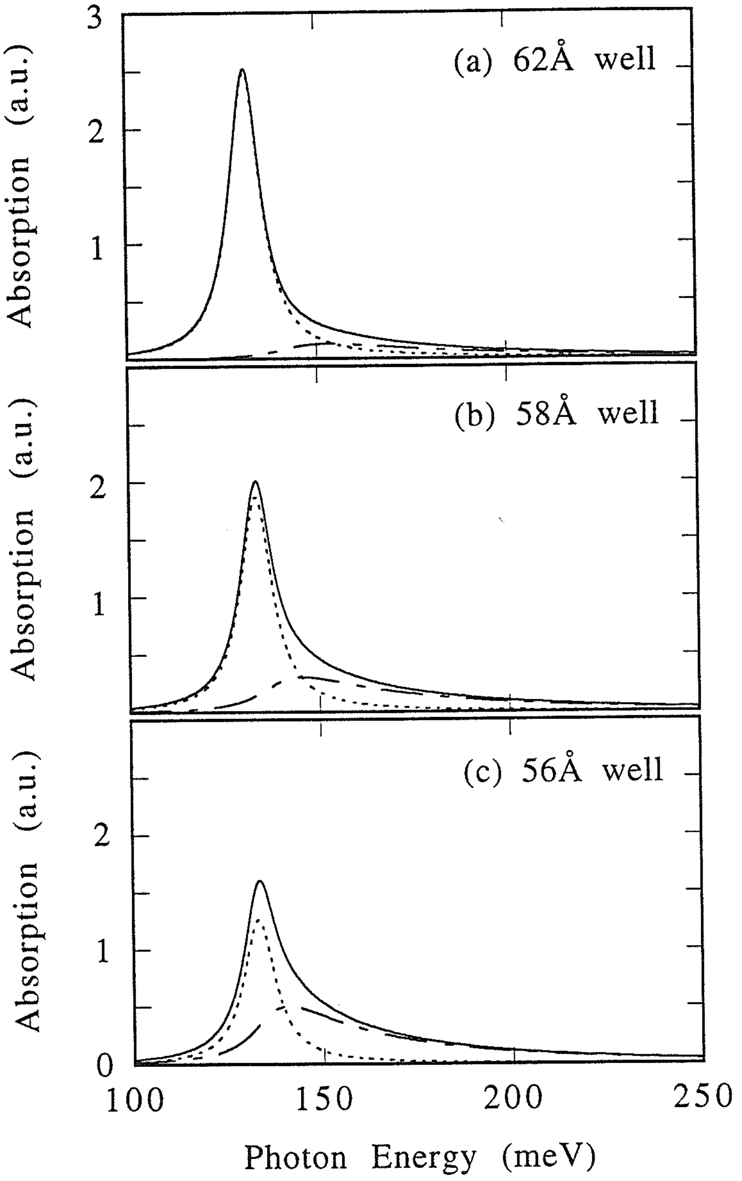

Figure 2.3: Theoretical absorption spectrum for bound-to-bound and bound-to-continuum transitions (dotted line is for bound-to-bound transition, dashed line is for bound-to-continuum transition, solid line is for the total absorption). The calculation is for SQW structure with $Al_{0.21}Ga_{0.79}As$ barriers and different GaAs well width.

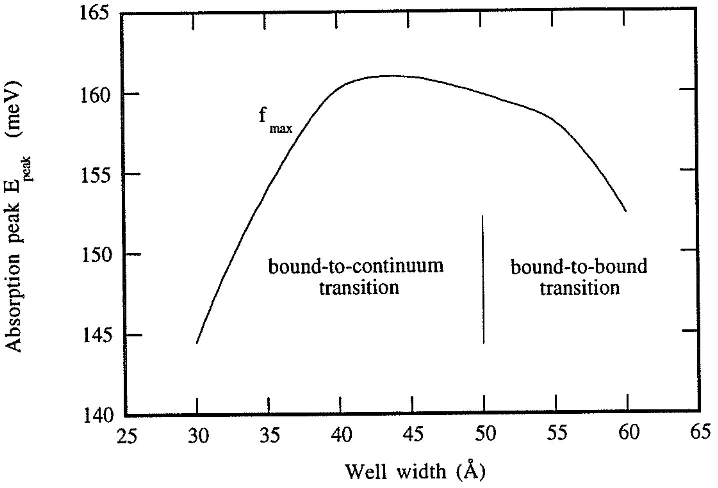

Figure 2.4: The absorption peak position versus well width for single quantum well structures with different GaAs well width and the same $Al_{0.25}Ga_{0.75}As$ barriers.

## 2.4 Mid-infrared absorption of bulk GaAs and air

The GaAs/AlGaAs quantum well structures studied in this thesis were grown on lattice matched GaAs substrates. We needed to look at the mid-infrared absorption of bulk GaAs in order to separate the properties of quantum well layers from the background. Semi-insulating GaAs substrates were used in all of our experiments because of the strong free carrier absorption in $n^+-$ GaAs substrates. As it can be seen from Figure 2.5, $n^+-$ GaAs is not transparent for wavelengths larger than 9.2 $\mu$m, while the absorption of semi-insulating GaAs is small for mid-infrared radiation from 2.4 $\mu$m to 12.4 $\mu$m. The absorption of $n^+-$ GaAs is, however, comparable to semi-

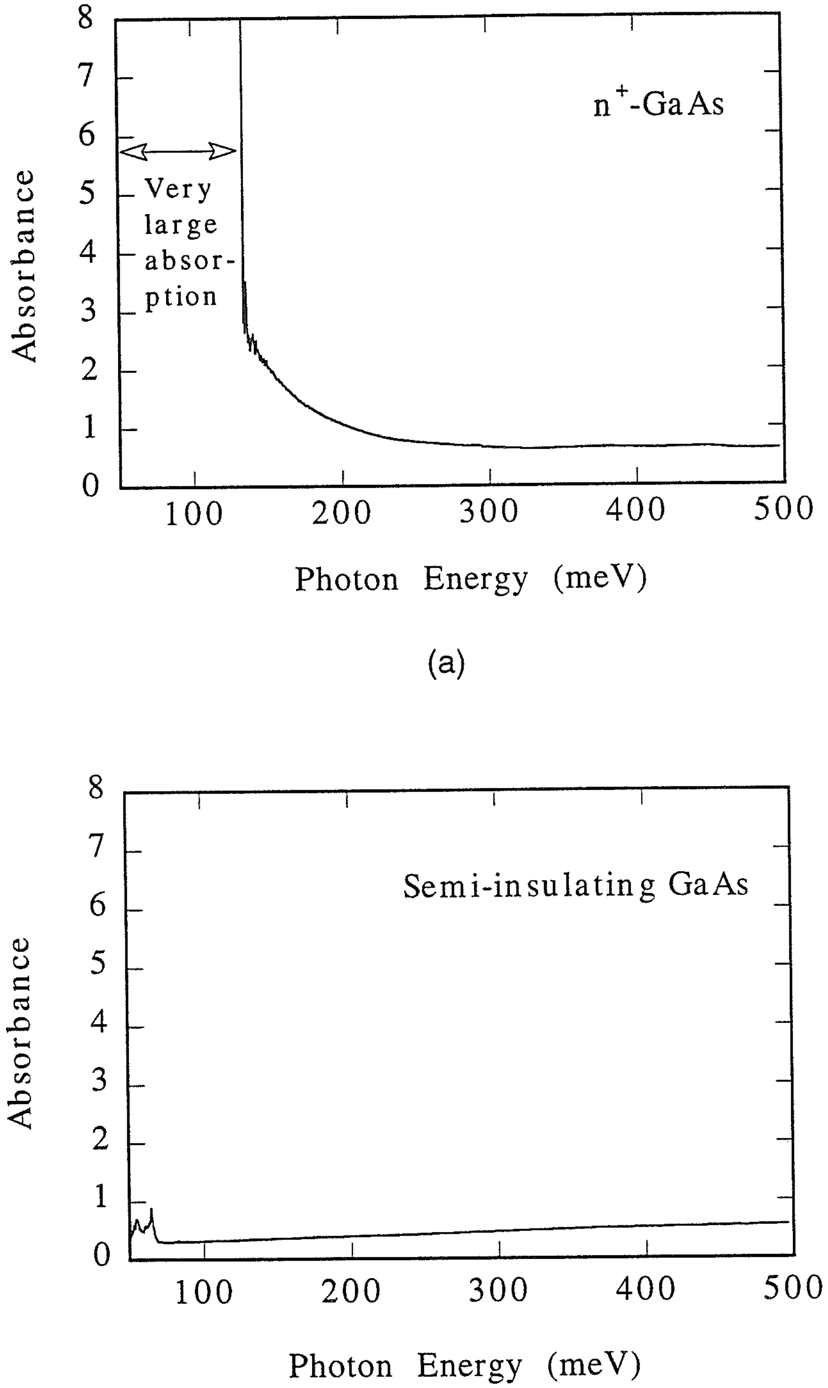

(a)

(b)

Figure 2.5: Absorbance spectra for (a) n$^+$− GaAs substrate and (b) semi-insulating GaAs substrate, where absorbance is defined in Chapter 4.

insulating GaAs in the wavelength range of 2.4 $\mu$m to 4 $\mu$m. Thus, for applications in this wavelength range, both substrates can be used.

Figure 2.6 shows that moisture ($H_2O$) and $CO_2$ in the air have absorption lines in the photon energy range of interest. Although their absorption is small, it is necessary to purge the experimental chamber with $N_2$ to eliminate extra absorption peaks due to moisture and $CO_2$.

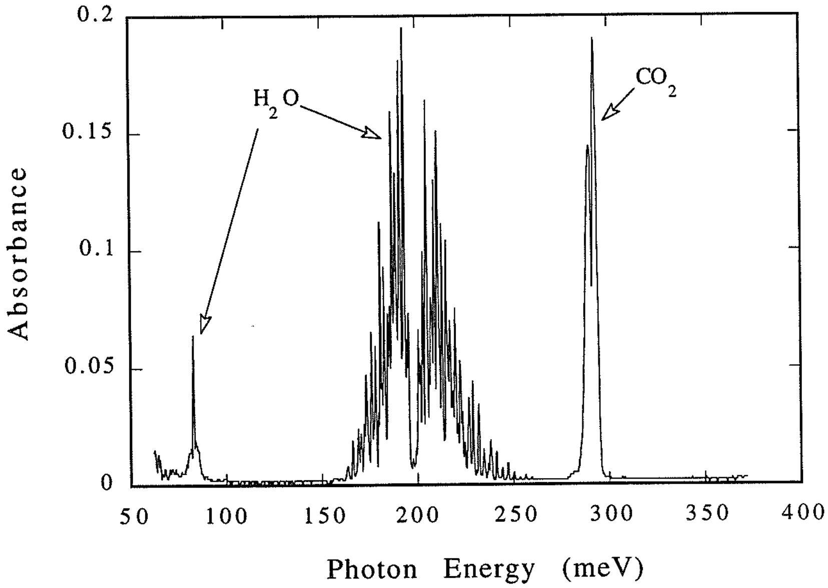

Figure 2.6: Air absorbance spectrum

## 2.5 Quantum well intersubband infrared photodetectors

The transition of electrons in the ground state of a quantum well structure to the excited state can be induced by infrared light. When a multiple quantum well structure (superlattice) is under external bias, the photo-excited electrons can either move in the quantum well plane (for applied bias parallel to this plane), or move perpendicularly to the quantum wells (for applied bias parallel to the crystal growth direction). For detector applications, transport in the crystal growth direction is chosen because the difference between the electron mobility for the ground state and for the excited state is large, so that the dark current can be reduced. If the photo-excited electrons can tunnel out of the quantum wells, they will contribute to the photocurrent. Since electrons in the biased structure can also be thermally excited to the continuum (thermionic emission) or tunnel through the barriers, there is an "inevitable" dark current which is generated. In the following sub-sections, we will look at the detector photoresponse and its dark current.

### 2.5.1 Detector photoresponse

The infrared detector sensitivity can be described by the amount of photocurrent generated to the incident optical power, which is called responsivity. The responsivity spectrum can be measured as described by Levine [10], Eisenman [11]. A dual lock-in ratio system is used to normalize the system spectral response. The absolute magnitude of the responsivity is determined by measuring the photocurrent with a calibrated globar blackbody source and a monochrometer. For the Fourier Transform Infrared spectrometer (FTIR spectrometer) used in this work, however, the photocurrent spectrum of a detector is used.

The blackbody spectral density [12] is

$$W(\Lambda) = 2\pi c^2 h \frac{\Lambda^3}{e^{hc\Lambda/k_B T} - 1}, \tag{2.14}$$

where $\Lambda = 1/\lambda$ is the wavenumber, $h = 2\pi\hbar$, $k_B$ is the Boltzmann constant, T is the absolute temperature of the blackbody source. The temperature of the globar blackbody source used in our experiment is 1000 K. Figure 2.7 shows the calculated blackbody spectral density. The radiation from an assumed 300 K blackbody is also shown in the figure for comparison. Notice that the spectral densities for the two different sources are in different scales. It is obvious that the radiation from the room temperature background can be neglected compared with that from an 1000 K blackbody source when the same infrared window is used.

For a given device, the total photocurrent can be measured from the differences in the I-V characteristics of the device under infrared illumination and in the dark. This total photocurrent can then be used to normalize the measured photoresponse spectrum from FTIR spectrometer (the integrated area of the measured photoresponse spectrum should be equal to the total measured photocurrent from I-V characteristics). If the infrared radiation incident on the detector is calibrated, then the detector responsivity can be measured/calculated from the calibrated radiation and measured

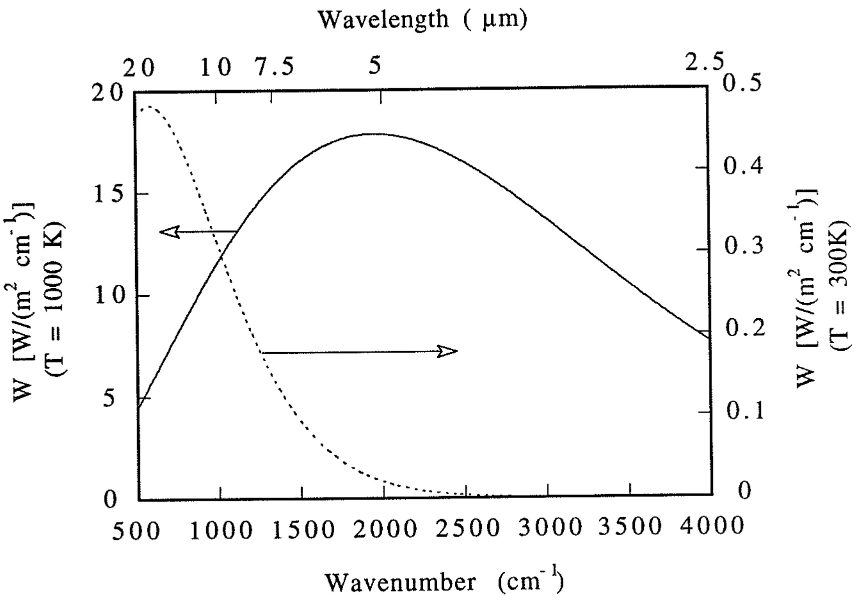

Figure 2.7: Blackbody radiation spectra.

photocurrent spectrum. The advantage of FTIR measurement is that the whole photocurrent spectrum can be measured at once. From Zussman's photocurrent expression [13],

$$I_p^{total} = \int_{\Lambda_1}^{\Lambda_2} I_p(\Lambda) d\Lambda \tag{2.15}$$

$$= \int_{\Lambda_1}^{\Lambda_2} R(\Lambda) P(\Lambda) d\Lambda, \tag{2.16}$$

where $\Lambda_1$ and $\Lambda_2$ are integration wavenumber limits that extend over the responsivity, $I_p(\Lambda) = R(\Lambda)P(\Lambda)$ is the photocurrent per unit wavenumber, $R(\Lambda)$ is the responsivity and $P(\Lambda)$ is the blackbody radiation power per unit wavenumber incident on the detector. $P(\Lambda)$ is given by

$$P(\Lambda) = W(\Lambda) \sin^2\left(\frac{\Omega}{2}\right) AC_F \cos\theta, \tag{2.17}$$

where $\Omega$ is the solid angle for the detector viewing the optical field, $A$ is the detector area, $C_F$ takes into account FTIR spectrometer optical system reflection, dewar window reflection, and the detector edge 45° mirror reflection and $\theta$ is the optical field incident angle referring to the quantum well plane. From the above two equations, we know

$$I_p(\Lambda) = R(\Lambda)W(\Lambda)\sin^2(\Omega/2)AC_F\cos\theta. \tag{2.18}$$

The unknown parameters in our experiment are $\Omega$ and $C_F$, both of which are independent from the device structure. So, we used the photocurrent spectrum $I_p(\Lambda)$ in the device analysis.

### 2.5.2 Dark current

As mentioned above, the three main mechanisms contributing to dark current are field-assisted and impurity-assisted tunneling and thermionic emission. To reduce the dark current, we used very thick barriers (~400 Å), so, the field-assisted tunneling can be neglected. For high quality molecular beam epitaxy (MBE) grown samples, one can usually ignore the contribution caused by impurities to the dark current at temperature higher than ~80 K. In this temperature range, the main contribution to dark current comes from thermionic emission or thermally-assisted tunneling which has been studied by Kinch and Yariv [14]. The dark current for quantum well infrared photodetectors can be expressed as:

$$I_d = An_tqv_d, \tag{2.19}$$

where $A$ is the device area, $n_t$ is carrier density contributing to the dark current and $v_d$ is electron drift velocity which will be assumed to be temperature independent [15]. The thermally excited carrier density $n_t$ is given by [14]

$$n_t = \frac{1}{L_p} \int_{E_o}^{\infty} T(E,V) f(E) \rho_{2D}(E) dE, \tag{2.20}$$

where $L_p$ is the MQW period, $T(E,V)$ is the bias-dependent transmission coefficient for a electron with energy $E$ tunneling through the barrier, $f(E)$ is the Fermi-Dirac distribution function. In the case of bound-to-continuum transitions, if we consider an effective barrier with potential $E_b$ varying with bias and approximate $T(E,V)$ by

$$T(E,V) = 0, \text{ for } E < E_b,$$

and

$$T(E,V) = 1, \text{ for } E > E_b,$$

then Equation (2.20) becomes

$$n_t = \frac{m^* k_B T}{\pi \hbar^2 L_p} \log\left(1 + e^{-(E_b - E_f)/k_B T}\right). \tag{2.21}$$

When the temperature is sufficiently high (but low enough such that $k_B T <<$ $(E_b - E_f)$), then

$$-\log\left(\frac{I_d}{T}\right) \propto \frac{E_b - E_f}{k_B T}. \tag{2.22}$$

To compare the dark current temperature dependence with the above equation, a stack of GaAs/AlGaAs MQWs was grown by MBE on (100) semi-insulating GaAs substrate [19]. The structure consisted of, from the substrate to the surface, 0.6$\mu$m

$n^+-$GaAs bottom contact layer, 40 periods of 53 Å GaAs well layers sandwiched by 440 Å $Al_{0.24}Ga_{0.76}As$ barrier layers, and a 0.3$\mu$m $n^+-$GaAs top contact layer. The center 47 Å in each well was uniformly doped with Si. Following the MBE growth, circular mesas with 200$\mu$m diameter were defined by wet chemical etching. AuGe/Ni/Au was deposited onto the top and bottom $n^+-$GaAs layers to make ohmic contacts. Due to the intersubband transition selection rule, a 45° mirror was polished on the edge of the sample to couple incident infrared radiation for the photoresponse spectrum measurement.

These devices have a peak in photoresponse spectrum at 1207 $cm^{-1}$, as shown in Figure 2.8. The long wavelength cutoff frequency (frequency at half-peak strength) is 1118 $cm^{-1}$ (i.e., $E_b - E_o = 1118$ $cm^{-1}$). Figure 2.9 shows the dark current as a function of voltage at different temperatures (77 – 160 K). At these temperatures, the dark current is dominated by thermal current. Figure 2.10 shows the normalized dark current ($I_d/T$) as a function of inverse temperature for two different voltages. It can be seen that the exponential fit is very good over 4 orders of magnitude of current change. The slope of the line in Figure 2.10 corresponds to $(E_b - E_f)$ for a given bias voltage. $(E_b - E_f)$ is plotted as a function of voltage drop per period (V) in the Figure 2.11. As expected, the effective barrier height seen by electrons going out of the quantum well is decreasing as the applied bias increases. But it does not show linear dependence, in contrast to the recent study by Lee et al. [20]. This barrier lowering effect, which has been introduced phenomenologically by Levine et al. [18] to explain carrier escape probability out of the quantum wells under different biases, is thus measured directly. In addition, the peak position is not at 0 volt, which is due to doping segregation during MBE growth of the sample [20,21].

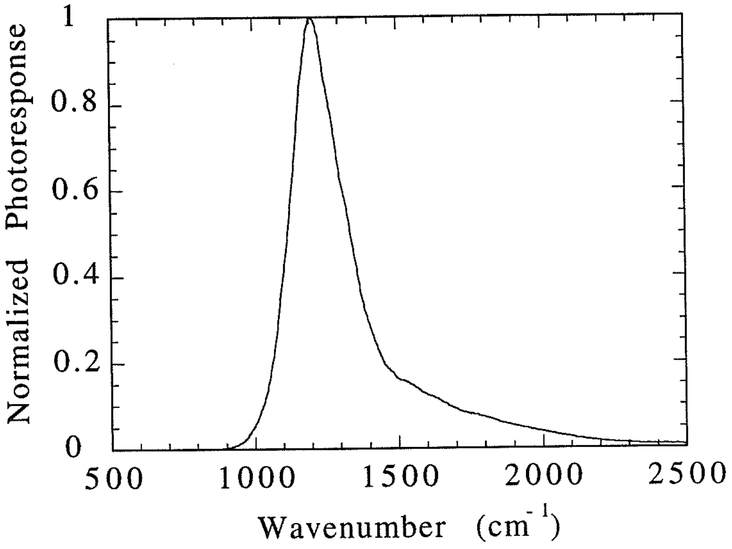

Figure 2.8: Normalized photoresponse of the detector under $V_{bias} = -2V$ at T = 10 K. The bias polarity is defined with the bottom contact as ground.

## 2.6 Conclusion

Electronic subbands and intersubband absorption were described. Simple quantum well structures can be used in photodetectors with a small tuning range of intersubband transition energies. The chapter also described intersubband transition selection rules and oscillator strength sum rule. The absorption feature of bulk GaAs and air background can be separated from that of superlattices. Detector photoresponse and

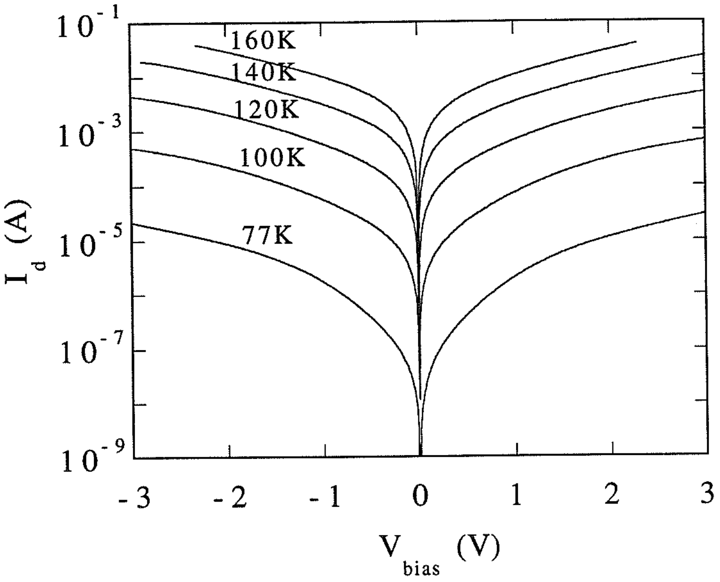

Figure 2.9: Measured dark I-V characteristics of the detector at different temperatures.

dark current were reviewed and discussed. In addition, it was shown that the normalized dark current had an exponential dependence on the inverse temperature over four orders of magnitude change of current when the dark current was dominated by thermionic emission in a bound-to-continuum quantum well structure.

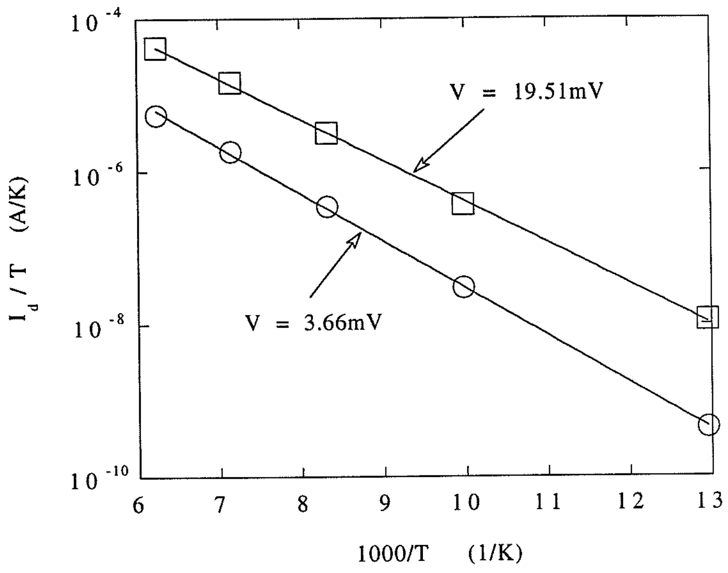

Figure 2.10: Normalized dark current $(I_d/T)$ versus inverse temperature for two values of applied bias per period. Experimental data are indicated as points.

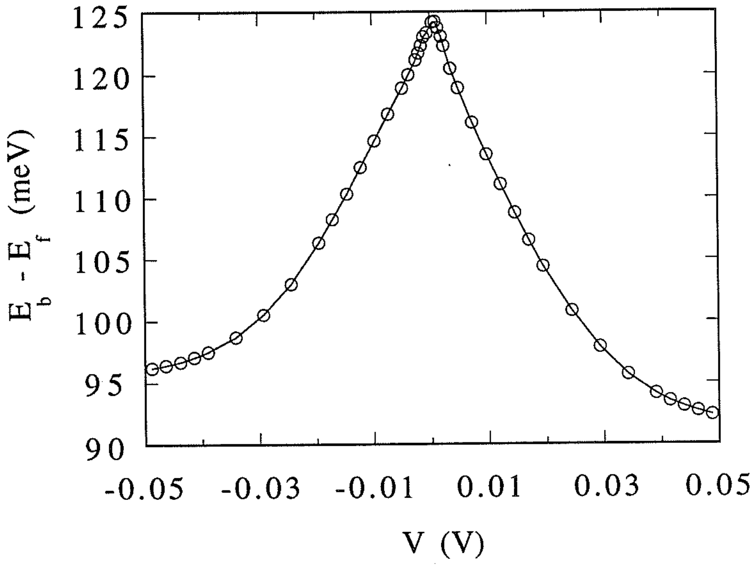

Figure 2.11: Effective barrier height seen by electrons going out of the quantum wells ($E_b - E_f$) versus bias voltage per period. $E_b - E_f$ is calculated from the slope of the straight line for each bias in Figure 2.10.

# References

[1] G. Bastard, Wave Mechanics Applied to Semiconductor Heterostructures, Halstead Press, 1988.

[2] A. Yariv, Quantum Electronics, New York: John Wiley and Sons, $3^{rd}$ edition, 1989.

[3] C. Sirtori, F. Capasso, J. Faist, S. Scandolo, "Nonparabolicity and a sum-rule associated with bound-to-bound and bound-to-continuum intersubband transitions in quantum-wells," Phys. Rev. B, vol. 50, no. 12, pp. 8663-8674, 1994.

[4] J. Y. Andersson, L. Lundqvist, J. Borglind, and D. Haga, "Performance of grating coupled AlGaAs/GaAs quantum well infrared detectors and detector arrays," Quantum Well Intersubband Transition Physics and Devices, edited by H. C. Liu, B. F. Levine, and J. Y. Andersson, vol. 270, pp. 13-28, 1993.

[5] K. K. Choi, M. Taysing-Lara, P. G. Newman, and W. Chang, "Wavelength tuning and absorption line shape of quantum well infrared photodetectors," Appl. Phys. Lett., vol. 61, no. 15, 1992.

[6] K. S. Yi and J. J. Quinn, "Optical absorption and collective modes of surface space-charge layers on (110) and (111) silicon," Phys. Rev. B, vol. 27, no. 4, pp. 2396-2411, 1983.

[7] T. Cole and B. D. McCombe, "Intersubband spectroscopy and valley degeneracy of Si(110) and Si(111) $n-$type inversion layers," Phys. Rev. B, vol. 29, no. 6, pp. 3180-3192, 1984.

[8] C. L. Yang, D. S. Pan, and R. Somoano, "Advantages of an indirect semiconductor quantum well system for infrared detection," J. Appl. Phys. vol. 65, no. 8, pp. 3253-3258, 1989.

[9] Y. H. Wang, S. S. Li, P. Ho, and M. O. Manasreh, "A normal incidence type-II quantum well infrared photodetector using an indirect AlAs $\mathrm{Al_{0.5}Ga_{0.5}As}$ system grown on (110) GaAs for midwavelength and long wavelength multicolor detection," J. Appl. Phys., vol. 74, no. 2, pp. 1382-1387, 1993.

[10] B. F. Levine, C. G. Bethea, G. Hasnain, J. Walker, and R. J. Malik, "High-detectivity $D^* = 1.0 \times 10^{10} cm\sqrt{Hz}/W$ GaAs/AlGaAs multiquantum well $\lambda = 8.3\mu$m infrared detector," Appl. Phys. Lett., vol. 53, no. 4, pp. 296-298, 1988.

[11] W. L. Eisenman, J. D. Merriam, and R. F. Potter, "Operational characteristics of infrared photodetectors," in Semiconductors and Semimetals, vol. 12, edited by R. K. Willardson.

[12] R. H. Kingston, Detection of Optical and Infrared Radiation (Springer, Berlin, 1978).

[13] A. Zussman, B. F. Levine, M. Hong, and J. P. Mannaerts, "GaAs/$Al_xGa_{1-x}As$ quantum well infrared photodetectors with cutoff wavelength $\lambda_c = 14.9\mu m$," Electron. Lett., vol. 27, no. 17 , pp. 1512-1513, 1991.

[14] M. A. Kinch and A. Yariv, "Performance limitations of GaAs/AlGaAs infrared superlattices," Appl. Phys. Lett., vol. 55, no. 20, pp. 2093-2095, 1989.

[15] M. L Lovejoy, M. R. Melloch, and M. S. Lundstrom, "Temperature dependence of minority and majority carrier mobilities in degenerately doped GaAs," Appl. Phys. Lett., vol. 67, no. 8, pp. 1101-1103, 1995.

[16] B. F. Levine, C. G. Bethea, G. Hasnain, V. O. Shen, E. Pelve, R. R. Abbott, and S. Hsieh, "High-sensitivity low dark current 10 $\mu$m GaAs quantum well infrared photodetectors," Appl. Phys. Lett., vol. 56, no. 1, pp. 851-853, 1990.

[17] S. R. Andrews and B. A. Miller, "Experimental and theoretical studies of the performance of quantum-well infrared photodetectors," J. Appl. Phys., vol. 70, no. 1, pp. 993-1003, 1991.

[18] B. F. Levine, C. G. Bethea, K. K. Choi, J. Walker, and R. J. Malik, "Tunneling lifetime broadening of the quantum well intersubband photoconductivity spectrum," Appl. Phys. Lett., vol. 53, no. 1, pp. 231-233, 1988.

[19] Y. Xu, A. Shakouri, A. Yariv, T. Krabach, and S. Dejewski, "Direct measurement of doping density and barrier lowering effect with bias in quantum wells," Elect. Lett., vol. 31, no. 4, pp. 320-321, 1995.

[20] C. Y. Lee, M. Z. Tidrow, K. K. Choi, W. H. Chang, and L. F. Eastman, "Activation characteristics of a long wavelength infrared hot-electron transistor," Appl. Phys. Lett., vol. 65, no. 1, pp. 442-444, 1994.

[21] E. C. Larkins, H. Schneider, S. Ehret, J. Fleissner, B. Dischler, P. Koidl, and J. D. Ralston, "Influence of MBE growth-processes on photovoltaic 3-5 $\mu$m intersubband photodetectors," vol. 41, no. 4, pp. 511-518, 1994.

# Chapter 3

# Numerical solution to Schrödinger's and Poisson's equations

To design prescribed electrical and optical response or to interpret the electrical and optical properties of quantum well devices, it is important to develop a quantitative theory. In simple quantum well structures, analytical equations can be used to describe electronic states as discussed in Chapter 2. In this chapter, we will first present the theoretical formulations used in the self-consistent calculation of general quantum well structures. The inclusion of the many-body effects in the single electron Schrödinger's equation has been justified by Ando [1] and Stern [2]. We limit ourselves to the discussion of the one-dimensional case, which is appropriate for the mid-infrared devices used for our study because of the large lateral device size.

This simplifies the numerical problem, and allows the implementation of a complex theoretical model. Only time-independent phenomena will be discussed. To solve Schrödinger's equation with arbitrary one-dimensional potential, we use the transfer matrix method. Some numerical examples are then presented.

## 3.1 Theoretical formulations

In the calculation of subband energy levels of quantum well structure in the inversion layer of a MOSFET using Schrödinger's equation and Poisson's equation, it has been shown that it is important to include the exchange-correlation energy for densities higher than $10^{11}$ cm$^{-2}$ [1]. Since the intersubband absorption is proportional to the subband population (see Equation (2.13)), high doping density is generally used in detector applications. Stern et al. [2], and Bloss [3] demonstrated that the Hartree potential, the local exchange-correlation energy, the exciton effect, the depolarization effect, and the external applied electric field are all non-negligible effects in order to make comparisons with experiment. The exciton shift is the interaction of the excited electron with the hole left in the ground state, similar to the interaction of electron-hole pairs in the conduction-valence band. The depolarization shift is a plasma shift of the transition caused by the screening of the electron gas. The effective mass Schrödinger equation within the envelope approximation framework is given by Equation (2.2). The term $V(z)$ in the equation is now the total potential including the barrier potential $V_0(z)$, the Hartree potential $V_H(z)$, the local exchange-correlation potential $V_{xc}(z)$ which takes the many-body effects into account, and the contribution of the externally applied field $F$,

$$V(z) = V_0(z) + V_H(z) + V_{xc}(z) + qFz. \tag{3.1}$$

## Hartree potential

The Hartree potential is calculated from the self-consistent solution to Poisson's equation and Schrödinger's equation. When the Hartree potential for electrons is in units of volts, the Poisson equation takes the form:

$$\frac{d}{dz}\left(\epsilon_r(z)\frac{dV_H}{dz}\right) = \frac{q}{\epsilon_0}[N_D^+(z) - n(z)], \tag{3.2}$$

where $N_D^+(z)$ is the density of ionized donors, the electron local three-dimensional density is given by [6]

$$n(z) = \frac{k_B T}{\pi\hbar^2}\sum_i M_i^* \log\left[1 + \exp\left(\frac{E_F - E_i}{k_B T}\right)\right] |\psi_i(z)|^2,$$

where $M_i^*$ is the i$^{th}$ subband average effective mass given by

$$M_i^* = \left[\int_{-\infty}^{+\infty} \frac{|\psi_i(z)|^2}{m_i^*(z)} dz\right]^{-1},$$

assuming that $\psi_i(z)$ has been normalized, $\int_{-\infty}^{+\infty} |\psi_i(z)|^2 dz = 1$.

## Exchange-correlation potential

In accordance with the theory of Hohenberg et al. [4], the exchange-correlation potential is generally an unknown functional of the electron density $n(z)$. In the local density approximation, $V_{xc}$ has been given different forms with similar quantitative results for subband energy level by a number of authors [2,3,5]. Following Stern et al. [2], the local exchange-correlation potential is

$$V_{xc}(z) = -\left[1 + \frac{0.7734}{\xi}\log(1+\xi)\right]\frac{\xi}{10.5\pi\alpha}R_y^*, \tag{3.3}$$

where

$$\alpha = \left(\frac{4}{9\pi}\right)^{1/3},$$
$$\xi = 21\left(\frac{4}{3}\pi a^{*3}n(z)\right)^{1/3},$$
$$a^* = \frac{4\pi\epsilon_0\epsilon_r(z)\hbar^2}{m^*(z)e^2},$$

$\epsilon_r(z)$ is the local relative dielectric constant. $R_y^*$ in Equation (3.3) is the effective Rydberg, $R_y^* = e^2/(8\pi\epsilon_0\epsilon_r(z)a^*)$. The charge-image interaction is neglected in calculating $V_{xc}$ because the change in the dielectric constant is on the order of 10% or less for GaAs-Al$_x$Ga$_{1-x}$As heterostructures and thus the image interaction is much smaller than the direct Coulomb interaction.

## Depolarization and exciton shift

The intersubband transition energies are also affected in the absorption process by the exciton and depolarization effects. These effects are included in our calculation using the formalism of Ando [7]. The intersubband transition energies ($\Delta E_0$) are shifted to

$$\Delta E = \Delta E_0\sqrt{1+\kappa-\beta}, \tag{3.4}$$

where $\kappa$ takes depolarization effect into account and is given by

$$\kappa = \frac{2q^2 n_{2D} S_{0i}}{\epsilon_r \epsilon_0 \Delta E_0},$$

$S_{0i}$ is the Coulomb matrix element given by

$$S_{0i} = \int_{-\infty}^{+\infty} dz \left( \int_{-\infty}^{z} dz' \psi_i(z') \psi_0(z') \right)^2,$$

and $\beta$ accounts for the exciton effect and is given by

$$\beta = -\frac{2n_{2D}}{\Delta E_0} \int_{-\infty}^{+\infty} dz \psi_i(z)^2 \psi_0(z)^2 \frac{\partial V_{xc}[n(z)]}{\partial n(z)}.$$

## 3.2 Boundary conditions

When a given potential is applied across a quantum well structure, Dirichlet boundary conditions should be used, and the corresponding electric field is calculated from the self-consistent calculation. We can also use the Neumann boundary conditions for a given external applied field and deduce the bias through the self-consistent calculation. Although both boundary conditions can be used, inappropriate physical considerations for the boundary exists in published literature [8]. (In Reference [8], the potential of the doped barriers can not be taken as constant.) Periodic boundary conditions are not considered because of the short coherence length of electrons except where indicated.

## 3.3 Transfer matrix method

There are several numerical methods, such as transfer matrix, finite difference, shooting, finite element, etc., to solve Schrödinger's and Poisson's equations. In solving the problem of complex energy (for quasi-bound state), the transfer matrix method was chosen because of its simplicity. Later on, the method was developed to do the self-consistent calculation. For some cases, such as in the absorption coefficient calculation of bound-to-continuum transitions (which will be discussed in Chapter 4), the advantage of transfer matrix method is that the accuracy of the numerical solutions does not depend on the mesh size, which can not be done using other numerical methods.

We will discuss the transfer matrix technique in the context of solving the Schrödinger equation. The technique can also be applied to solve other differential equations, e.g., the Poisson equation. The transfer matrix technique consists of dividing the quantum well structure with complicated potential profile into a number of intervals such that in each interval the potential can be approximated by either a constant or a linearly varying function. The envelope function in each interval is then given by the linear combination of two plane waves or two Airy functions. We consider the case of a constant potential in each interval as shown in Figure 3.1.

The potential profile is discretized into $N+1$ intervals where the first and the last intervals are assumed to have constant potential and to extend to infinity away from the quantum well structure. In the $i^{th}(i = 1, \ldots, N+1)$ interval, the envelope

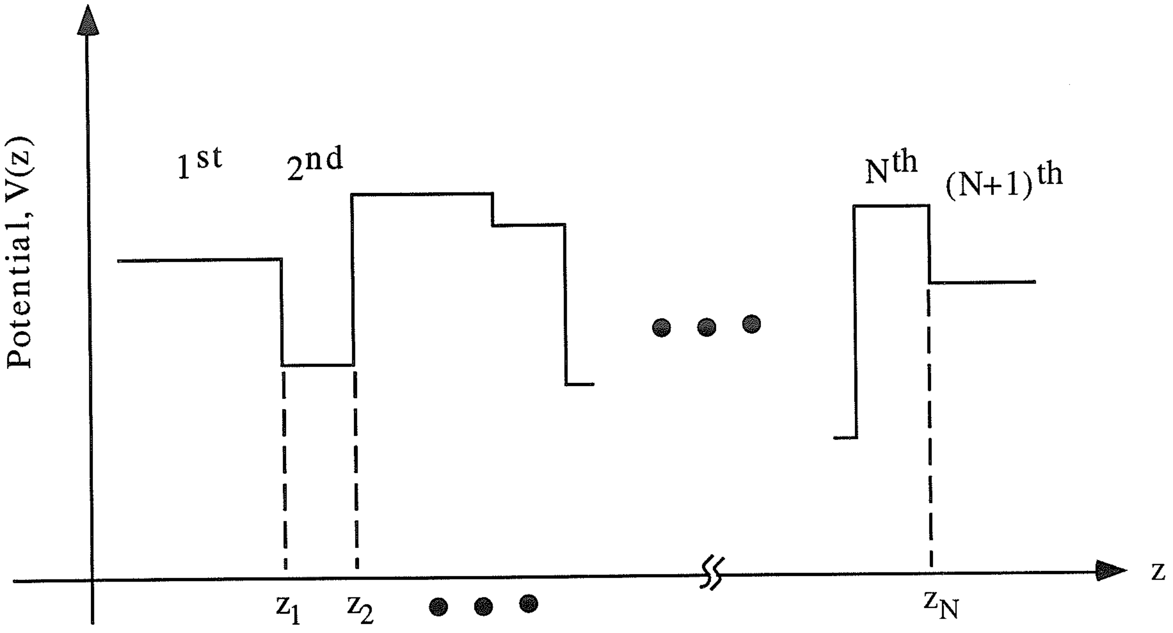

Figure 3.1: Schematic figure of discretized constant potentials versus the position.

function is given by

$$\psi_i(z) = A_i \exp[-k_i(z - z_{i-1})] + B_i \exp[k_i(z - z_{i-1})], \tag{3.5}$$

where $k_i = \sqrt{2m_i^*(V_i - E)}/\hbar$, $A_i$ and $B_i$ are complex constants to be determined from the boundary conditions and the normalization conditions for the envelope functions, $E$ is the eigenvalue.

The boundary conditions for the envelope functions at the border between two neighboring intervals can be expressed as

$$\psi_i(z_i) = \psi_{i+1}(z_i), \tag{3.6}$$

$$\left.\frac{1}{m_i^*}\frac{d\psi_i}{dz}\right|_{z=z_i} = \left.\frac{1}{m_{i+1}^*}\frac{d\psi_{i+1}}{dz}\right|_{z=z_i}. \tag{3.7}$$

The factor $1/m^*$ in Equation (3.7) is due to the conservation of particle current and ensures stationary eigenstates when there is a discontinuity in the effective mass at the boundaries as discussed by White et al. [9], and Bastard [10].

Applying the boundary conditions of Equations (3.6) and (3.7) to Equation (3.5), the coefficients $A_{i+1}$ and $B_{i+1}$ in the $(i+1)^{th}$ interval are related to the coefficients $A_i$ and $B_i$ in the $i^{th}$ interval as

$$\begin{pmatrix} A_{i+1} \\ B_{i+1} \end{pmatrix} = \mathrm{C}_i \cdot \begin{pmatrix} A_i \\ B_i \end{pmatrix}, \tag{3.8}$$

where $\mathrm{C}_i$ is given by

$$\mathrm{C}_i = \frac{1}{2}\begin{pmatrix} (1+\xi_i)\exp[-k_i(z_i - z_{i-1})] & (1-\xi_i)\exp[k_i(z_i - z_{i-1})] \\ (1-\xi_i)\exp[k_i(z_i - z_{i-1})] & (1+\xi_i)\exp[-k_i(z_i - z_{i-1})] \end{pmatrix}$$

with $\xi_i = (m^*_{i+1}/m^*_i)(k_i/k_{i+1})$. Repeating the analysis, we can find the following relation for $A_{N+1}$ and $B_{N+1}$ with $A_1$ and $B_1$

$$\begin{pmatrix} A_{N+1} \\ B_{N+1} \end{pmatrix} = \left(\prod_{i=N}^{1} \mathrm{C}_i\right) \cdot \begin{pmatrix} A_1 \\ B_1 \end{pmatrix} \tag{3.9}$$

$$= \begin{pmatrix} \mathrm{D}_{11} & \mathrm{D}_{12} \\ \mathrm{D}_{21} & \mathrm{D}_{22} \end{pmatrix} \cdot \begin{pmatrix} A_1 \\ B_1 \end{pmatrix}. \tag{3.10}$$

For bound states, the integral of the envelope function absolute square over the whole space should be finite, which requires that $A_1 = 0$, $z \in (-\infty, z_1]$ and $B_{N+1} = 0$, $z \in [z_N, +\infty)$. This constraints $\mathrm{D}_{22}$ in Equation (3.10) to be zero. The solution to

$$\mathrm{D}_{22}(E) = 0 \tag{3.11}$$

is the bound state energy.

To solve self-consistently Schrödinger's and Poisson's equations, we start with an approximate potential distribution. For example, we only include the barrier potential $V_0(z)$ and the external field contribution $eFz$ in the Schrödinger equation in the first iteration. The solution gives us the quantized energy levels $E_i^{old}$ and the electronic envelope functions. The Hartree potential is then obtained from the Poisson equation. In the second iteration, a new approximate potential profile $V^{new}(z)$ (including the Hartree potential and the local exchange-correlation potential) is used in the Schrödinger equation, the new quantized energy levels $E_i^{new}$ are then calculated. If $E_i^{new}$ agrees with $E_i^{old}$ within acceptable limits after several iterations, a self-consistent solution has been found. Otherwise, another iteration is employed. Mathematically,

$$V^{new,(n+1)}(z) = V^{old,(n)}(z) + g^{(n+1)} \cdot (V^{new,(n)}(z) - V^{old,(n)}(z))$$

where n represents the number of iterations, g is a convergence control factor and is independent of position z. The factor g is within the range of 0 to 1 and is chosen from experience. In some cases, rapid convergence can be obtained for g = 1.

## 3.4 Numerical examples

### 3.4.1 Miniband structure in superlattices

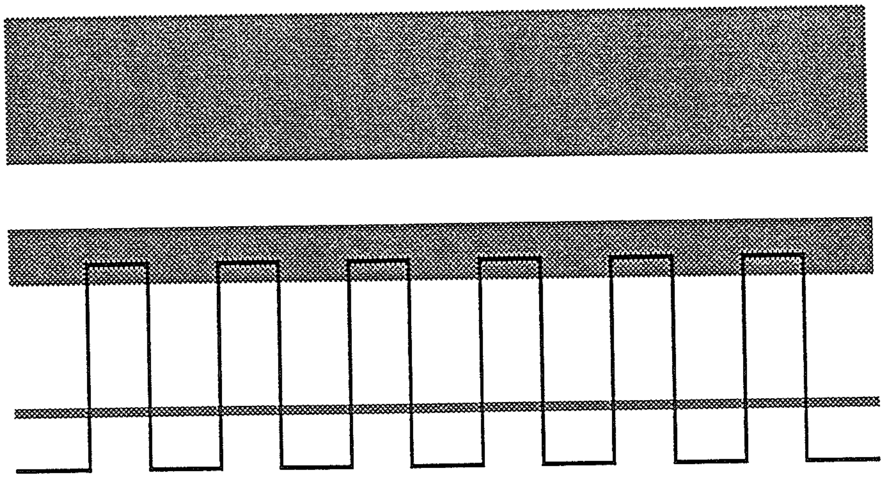

Figure 3.2: Quantum well structure with periodic potential distribution.

The first numerical example is to use transfer matrix method to calculate the miniband structure in superlattices. It is well known that there exist minibands in a superlattice when the potential has spatial translational symmetry. This miniband structure can also be calculated using the Kronig-Penny model. From this model, the miniband $E-k$ dispersion relation is given by the following two equations [11] for the case of a simple superlattice structure shown in Figure 3.2.

For $V > E$,

$$\cos(k(w+b)) = \cos(k_w w)\cosh(k_b b) - \frac{1}{2}\left(\xi - \frac{1}{\xi}\right)\sin(k_w w)\sinh(k_b b), \tag{3.12}$$

with

$$k_w = \frac{\sqrt{2m_w^* E}}{\hbar}, k_b = \frac{\sqrt{2m_b^*(V-E)}}{\hbar}, \xi = \frac{m_b^*}{m_w^*}\frac{k_w}{k_b};$$

for $V < E$,

$$\cos(k(w+b)) = \cos(k_w w)\cos(k_b b) - \frac{1}{2}\left(\xi + \frac{1}{\xi}\right)\sin(k_w w)\sin(k_b b), \tag{3.13}$$

with

$$k_w = \frac{\sqrt{2m_w^* E}}{\hbar}, k_b = \frac{\sqrt{2m_b^*(E-V)}}{\hbar}, \xi = \frac{m_b^*}{m_w^*}\frac{k_w}{k_b},$$

where $w$ is the well width, $b$ is the barrier thickness, $V$ is the barrier height. From Bloch's theorem, $\psi(z) = e^{ikz}u(z)$, where $k$ is the wave number of the envelope function in the z-axis and $u(z)$ is the periodic part in the envelope function at $k = 0$, $u(z) = u(z+w+b)$. The advantage of transfer matrix method is its flexibility in calculating eigen energies of any potential distribution. This allows us to study finite length superlattices as well.

Figure 3.3 shows minibands and miniband gaps for a simple periodic potential with 60 Å GaAs wells and 50 Å $Al_{0.22}Ga_{0.78}As$ barriers. The transmission coefficient spectrum for the same quantum well parameters but with only five periods is shown in Figure 3.4. The miniband gaps correspond to transmission coefficient close to 0.

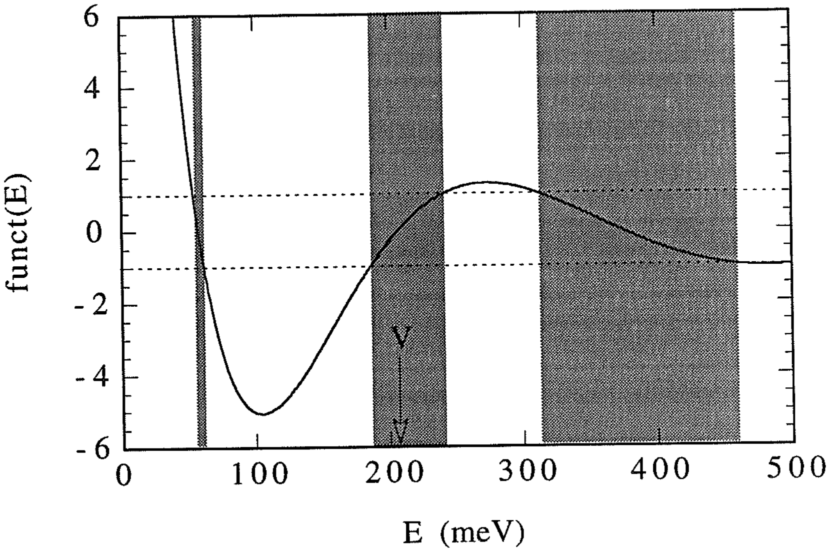

Figure 3.3: The right-hand side of Equations (3.11) and (3.12) is plotted versus the energy E for a periodic quantum well structure. The shaded area corresponds to the allowed states (minibands).

### 3.4.2 The influence of doping on the intersubband transition energy

The effect of doping density on the intersubband transition energy can be large. A change in the doping densities from $1 \times 10^{11}$ to $2 \times 10^{12}$ can change the transition energy by about 9 meV in a simple quantum well structure (assuming the barrier is undoped). The 9 meV correction to the intersubband transition energy is small compared with the intersubband transition energy in the mid-infrared range, but this correction is large when compared with the intersubband absorption linewidth.

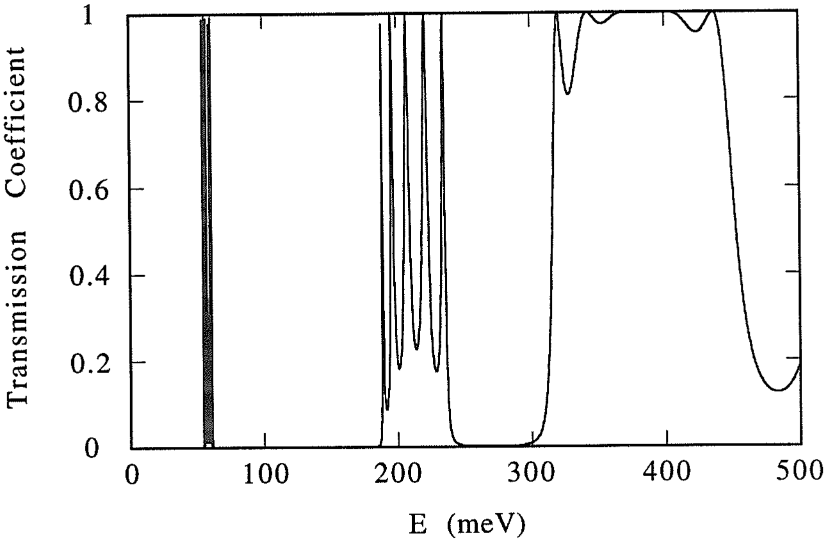

Figure 3.4: Transmission coefficient spectrum for a 5-period quantum well structure.

A theoretical example is shown in Figure 3.5 for a single quantum well structure with 75 Å uniformly doped GaAs well and undoped $Al_{0.25}Ga_{0.75}As$ barriers. The intersubband transition energy changes almost linearly with the doping density in this case. The self-consistent calculation included all terms in Equation (3.1).

### 3.4.3 The effect of external field, Hartree, and exchange-correlation interaction on intersubband transitions

Shown in Figure 3.6 is the theoretical calculation of Stark effect for a single quantum well structure with 82 Å GaAs well, where the center 50 Å is uniformly doped to $2\times10^{18}$ cm$^{-3}$, and undoped $Al_{0.4}Ga_{0.6}As$ barriers. The self-consistent calculation with Hartree and exchange-correlation interaction gives increased intersubband transition

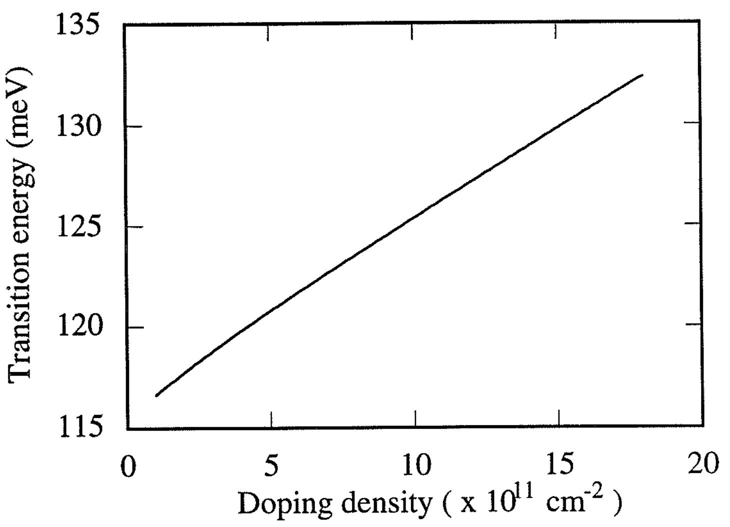

Figure 3.5: The intersubband transition energy versus the population in the well for a single quantum well structure.

energy. Depolarization and exciton shifts, acting to increase the transition energy, are also significant, and thus cannot be neglected in the theory. The Stark shift as shown in Figure 3.6(a), however, does not have noticeable change whether or not a self-consistent calculation is used. The small change of the oscillator strength with changing external field is shown in Figure 3.6(b).

Using an asymmetric quantum well structure to generate a large Stark effect has been proposed theoretically and demonstrated experimentally [12,13]. As an example, the effect of self-consistent calculation was studied for a step quantum well. This structure consisted of $Al_{0.34}Ga_{0.66}As$ barriers, 62 Å undoped $Al_{0.17}Ga_{0.83}As$ step barrier, and 62 Å selectively doped GaAs well. The selectively doped GaAs well was assumed to be Si doped to $2 \times 10^{18}$ $cm^{-3}$ in the center 50 Å. Figure 3.7(a) shows that the

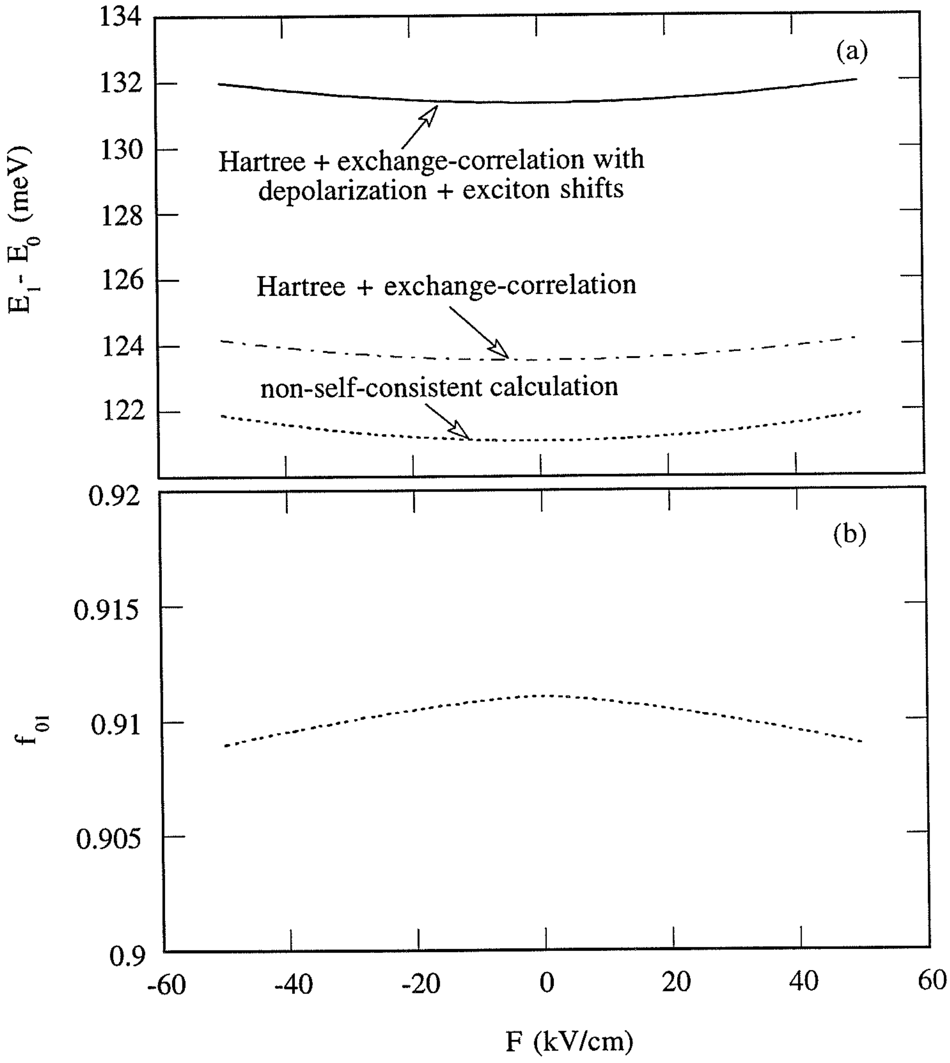

Figure 3.6: (a) Calculated intersubband transition energy and (b) oscillator strength versus external field.

Stark shift does not change significantly when the self-consistent calculation includes all effects, compared with the result from the non-self-consistent calculation. Again, the subband transition energy is strongly affected by Hartree, exchange-correlation interaction, and depolarization and exciton shifts. The oscillator strength depends on the external field strength and polarity as shown in Figure 3.7(b).

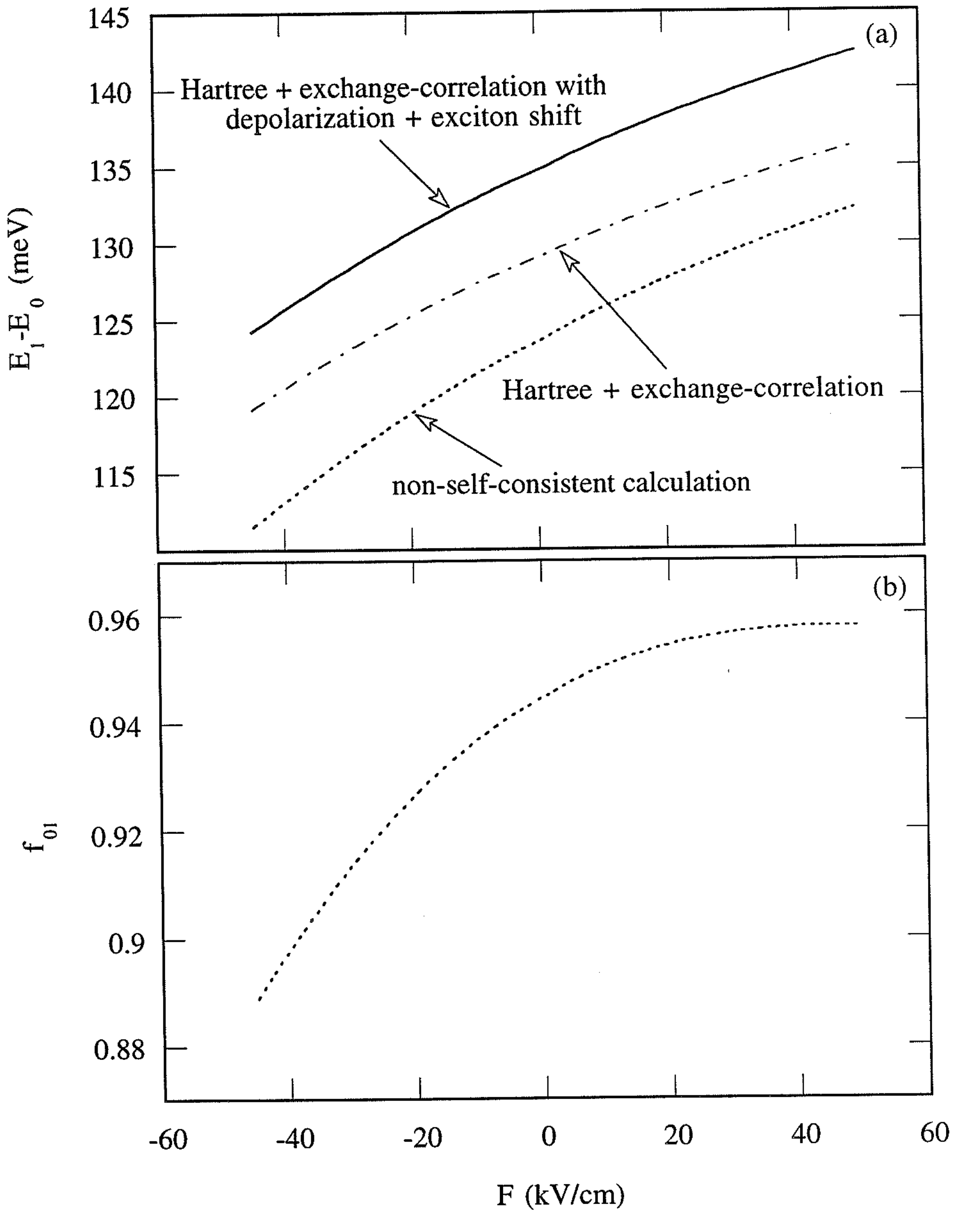

Figure 3.7: (a) Self-consistently and non-self-consistently calculated Stark effect for a step quantum well structure. (b) The oscillator strength versus external field.

## 3.5 Conclusion

The transfer matrix method can be used to solve Schrödinger's equation and Poisson's equation. This method has the advantage of solving bound-to-continuum transition problems without increasing the number of mesh points to get reasonable accuracy, and thus decreases the computational burden. It is necessary to perform self-consistent calculations to obtain intersubband transition energies with proper boundary conditions. Inclusion of external field, Hartree, exchange-correlation interaction, and depolarization and exciton shifts in the calculation of intersubband transition energy levels is important at high doping densities.

# References

[1] T. Ando, A. B. Fowler, and F. Stern, "Electronic properties of two-dimensional systems," Rev. Mod. Phys., vol. 54, no. 2, pp. 437-672, 1982.

[2] F. Stern and S. D. Dassarma, "Electron energy levels in GaAs-$Ga_{1-x}Al_xAs$ heterojunctions," Phys. Rev. B, vol. 30, no. 2, pp. 840-848, 1984.

[3] W. L. Bloss, "Effects of Hartree, exchange, and correlation energy on intersubband transitions," J. Appl. Phys., vol. 66, no. 8, pp. 3639-3642, 1989.

[4] P. Hohenberg and Kohn, Phys. Rev. B, vol. 136, p. 864, 1964.

[5] A. R. Williams and U. von Barth, "Theory of the inhomogeneous electron gas," edited by S. Lundqvist and N. H. March (Plenum, New York, 1983). U. von Barth, in "The electronic structure of complex materials" (NATO Advanced Study Institute, Ghent, 1982).

[6] G. Bastard, Wave Mechanics Applied to Semiconductor Heterostructures, Halsted press, 1988.

[7] T. Ando, "Intersubband optical transitions in a surface space-charge layer," Solid State Comm., vol. 21, no. 1, pp. 133-136, 1977.

[8] W. Q. Chen and T. G. Andersson, "Self-consistent analysis of electric field-dependent intersubband transitions for a thin layer inserted quantum well," J. Appl. Phys., vol. 73, no. 9, pp. 4484-4488, 1993.

[9] S. R. White, L. J. Sham, "Electronic properties of flat-band semiconductor heterostructures," Phy. Rev. Lett., vol. 47, no. 12, pp. 879-882, 1981.

[10] G. Bastard, "Superlattice band structure in the envelope-function approximation," Phys. Rev. B, vol. 24, no. 10, pp. 5693-5697, 1981.

[11] H. S. Cho and P. R. Prucnal, "New formalism of the Kronig-Penney model with application to superlattice," Phys. Rev. B, vol. 36, no. 6, pp. 3237-3242, 1987.

[12] P. F. Yuh, K. L. Wang, "Large Stark effects for transitions from local states to global states in quantum well structures," IEEE J. Quantum Electron., vol. 25, no. 7, pp. 1671-1676, 1989.

[13] Y. M. Huang, C. H. Lien, "Strong Stark-effect of the intersubband transitions in the 3 coupled quantum wells – application to voltage-tunable midinfrared photodetectors," J. Appl. Phys., vol. 78, no. 4, pp. 2700-2706, 1995.

# Chapter 4

# Quantum interference effect and electric field domain formation in quantum well infrared photodetectors

There have been a number of interesting experimental studies of the optical and transport properties of multiple quantum well (MQW) structures. In these "artificial molecules," energy quantization and the wave nature of carriers have been used to design new devices and to demonstrate some basic laws of quantum mechanics, e.g., to observe minibands in the continuum of periodic potential superlattice [1], to observe suppression of optical absorption in coupled potential wells [2], and to make quantum well infrared photodetectors (QWIPs) by using minibands in the continuum

[3]. Because of the short coherence length of electrons, most experimental work has been done using very short period of superlattices.

The electric field domain formation due to sequential resonant tunneling in a superlattice has been observed by the demonstration of the oscillatory behavior in the current-voltage characteristics of the superlattice. In this chapter, we describe the first observation of a quantum interference effect in the photocurrent spectrum of bound-to-continuum QWIPs. Using this effect, we analyze the electric field domain formation due to sequential resonant tunneling in the superlattice [4]. The effect of temperature on the resonant tunneling and electric field domain formation will also be described [5].

## 4.1 Quantum interference effect and electric field domain formation in QWIPs

### 4.1.1 Background

The electric field domain formation was first observed in bulk GaAs and is known as the Gunn effect, the the cause of Gunn oscillations [6]. The oscillation properties were explained through the negative differential resistance theory proposed by Kroemer [7]. In the Gunn effect, the field domains are generally spatially moving (there are cases that stable spatial field domains exist). The mechanisms causing the negative differential resistance in superlattices are different. The carriers are transported parallel to the crystal growth direction. Esaki and Chang [8] first observed the negative differential resistance in superlattices. The superlattice they used consisted of 45 Å GaAs wells and 40 Å AlAs barriers. Because of the strong coupling among neighboring wells, there were minibands, and the miniband width was large (5 meV miniband width for ground states). Electrons were transported through miniband conduction. Under external bias, negative differential conductance was observed when miniband conduction through ground states changed into one involving tunneling through ground state to higher states and subsequent relaxation to ground level. External bias made the ground state of one well aligned with the first excited state of its neighboring well in the high field domain for the first formation of domains. This was also observed by Choi et al. [9], who used weakly coupled quantum wells with bound-to-bound transitions. The superlattice used by Choi and his co-workers consisted of 49 periods of 76 Å GaAs wells with 88 Å $Al_{0.27}Ga_{0.73}As$ barriers. The miniband width for the ground states in this structure was ~0.4 meV and the quantum well states were localized (due to well width fluctuation or external field). Choi et al. observed very regular negative differential conductance oscillations from the I-V characteristics of their devices. Up to now, no moving electric field domains has been observed for the case of sequential resonant tunneling induced negative differential resistance in superlattices (when external bias is fixed). An optical experiment can be performed to study the formation of electric field domains in superlattices.

### 4.1.2 Quantum well infrared photodetector design

In a weakly coupled MQW structure with two bound states in each well (i.e. a bound-to-bound QWIP [3], such as the structure used by Choi et al. [9] as mentioned above), the absorption spectrum is a Lorentzian shaped peak corresponding to a transition between the ground state and the first excited state as shown in Figure 2.3(a). The contribution of other states in the continuum above the barriers is negligible because of the well-known oscillator strength sum rule (the zero-to-one transition has a much more significant transition dipole matrix element because both states are localized in the well).

When the quantum well parameters allow only one bound state in the well (i.e. a bound-to-continuum QWIP), the absorption spectrum is no longer Lorentzian, since many states above the barriers have a strong contribution to the absorption. Because these continuum states extend over the barriers and several neighboring wells (depending on the coherence length of electrons), electron interference effects can be observed in the absorption spectrum. At zero bias, due to the spatial translation symmetry of the potential there exist minibands in the continuum states of the superlattice [1] which can be calculated using the Kronig-Penney model or the transfer matrix method as discussed in the previous chapter. The miniband energy gaps, depending on the overlap of states between neighboring wells, can be designed large enough to be observable in the absorption spectrum. However, under an applied bias, such that the voltage drop per period is bigger than these energy gaps, the miniband structure is destroyed. We will show that in a QWIP even at large biases, one can still see some features in the photocurrent spectrum due to electron interference effects over one or two periods of the superlattice (~400 Å).

The sample investigated for this study was grown by molecular beam epitaxy (MBE) on a (100) semi-insulating GaAs substrate (Sample 1510). It consisted of 50 periods of 40 Å GaAs wells, separated by 200 Å $Al_{0.22}Ga_{0.78}As$ barriers. Each well was uniformly doped with Si to $n = 2 \times 10^{18}$ cm$^{-3}$, yielding a sheet density of $8 \times 10^{11}$ cm$^{-2}$.

### 4.1.3 Superlattice absorption characterization

After the MBE growth, the sample was polished mechanically on the bottom side. Small pieces (3 × 5 mm$^2$) were cleaved, and parallel 45° mirrors were polished on the two opposing ends to allow optical multiple pass transmission. The absorption measurement was performed using a Fourier Transform Infrared Spectrometer over the spectral range of 500 to 4000 cm$^{-1}$. The sample was mounted on a cold finger as shown in Figure 4.1. The linearly polarized radiation was incident normally on one of the 45° facets, and the transmitted radiation came out of the opposing facet. Due to the well-known intersubband transition selection rule, the absorbance was obtained from the ratio of the transmitted light intensity $I_{\perp}$ (corresponding to polarization perpendicular to the quantum well plane) to the transmitted light intensity

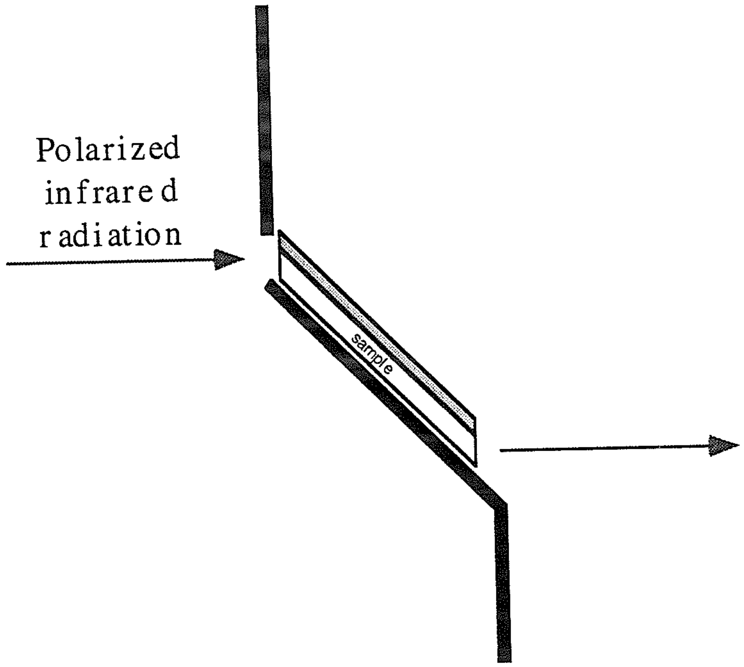

Figure 4.1: Schematic drawing for absorption spectrum measurement.

$I_{//}$ (corresponding to the polarization in the quantum well plane), that is,

$$\text{absorbance} = -\log_{10}\left(\frac{I_\perp}{I_{//}}\right). \tag{4.1}$$

The low temperature for the experimental absorption spectrum was achieved using an MMR (K-77) vacuum-assisted Joule-Thomson refrigerator by running high pressure nitrogen gas. The low temperature limit in this setup was 79 K. Figure 4.2 shows the experimental absorption spectrum. The theoretical curve was obtained by solving Schrödinger's and Poisson's equations in the envelope function approximation as discussed in Chapter 3. The effect of exchange-correlation was included through the one-particle exchange-correlation potential [10]. Non-parabolicity was taken into account as in Reference [11]. To treat the energy eigenstates above the barrier, the MQW structure was embedded between very large barriers at sufficiently large distances such that the far distant boundary conditions did not affect the calculated absorption spectra [12]. More than two superlattice periods were needed to fit the experimental results.

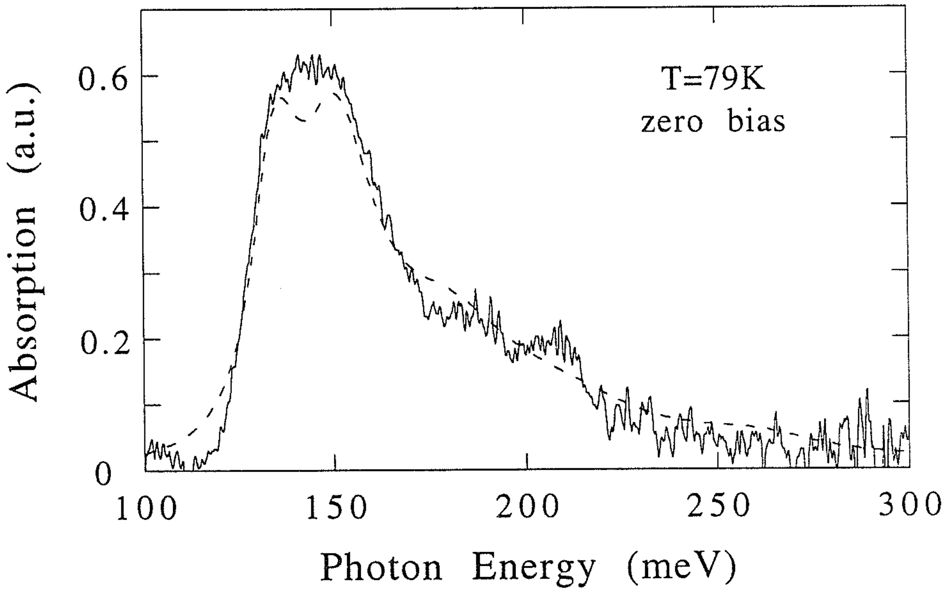

Figure 4.2: The experimental absorption spectrum at zero bias and T = 79 K (solid line), and the calculated absorption spectrum (dotted line).

### 4.1.4 Photoresponse spectrum

To measure the photocurrent spectrum, circular devices of 200 $\mu$m in diameter were defined by wet chemical etching. AuGe/Ni/Au was deposited onto the top and bottom $n^+$-GaAs contact layers. (The appropriate thicknesses of AuGe and Ni were chosen to give low contact resistance and shallow metal diffusion depth into GaAs layer according to Reference [13].) Forty-five degree mirrors were polished on the edges of the sample to couple incident infrared radiation in the measurement of the device photoresponse. Details of the device processing are described in Appendix A. The schematic drawing of the device is shown as Figure 4.3.

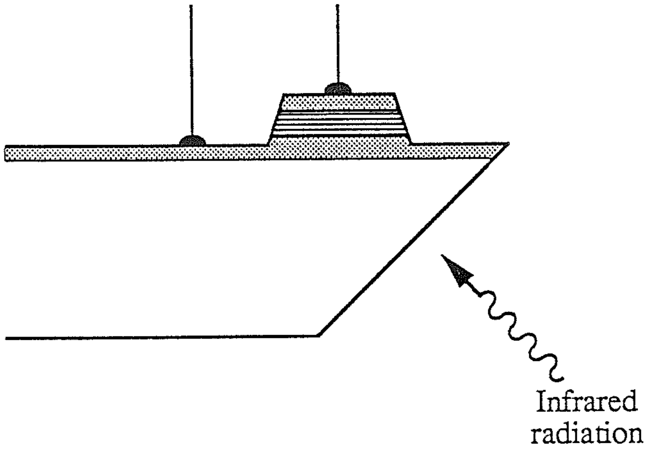

Figure 4.3: Schematic drawing of a device cross section.

Figure 4.4 shows the photocurrent spectrum at 10 K for an applied bias of -3 V (defined with respect to the bottom contact layer). Three peaks are evident at ~155, 187 and 220 meV in the photocurrent spectrum. The spacings of the peaks in the calculated absorption spectrum strongly depend on the applied field once the quantum well parameters are specified. The theoretical results show only two peaks in the absorption spectrum for a single quantum well. For a quantum well with its nearest neighbors in the superlattice, there are three peaks, as shown in Figure 4.4. The assumed electric field in the structure is ~31 kV/cm for both of these curves.

This clearly shows that the observed peaks in the photocurrent spectrum originate from electron interference effects over at least one superlattice period (a distance of more than 240 Å).

Although the superlattice minibands (in the Kronig-Penney sense) are destroyed at these applied biases, the physical origin of these observed peaks is that the dipole matrix element, which is basically an overlap integral between the *localized* ground state in the well and the excited states above the barrier, possesses peaks (resonances) reflecting interference over neighboring wells. Alternatively, this can be viewed as the *local* density of the states (i.e. density of states normalized by the amplitude of the wavefunction in the well region) having peaks. The total density of states, which shows the energy level spacings for the whole superlattice, may not have any noticeable structure.

One notices that even though the *position* and the *spacing* of the peaks in the theoretical absorption spectrum match the experimental photocurrent spectrum, it is impossible to fit them together exactly (especially in the low energy region). This is because the photocurrent spectrum involves additional effects due to electron emission from the quantum well, transport in the superlattice, and capture in a distant quantum well or in the contact layers [14]. The energy dependence of these additional processes will affect the photocurrent spectrum.

To further substantiate the fact that these observed peaks in the photocurrent spectrum originate from the local density of states in the well region and reflect electron coherence over a few periods of the superlattice, a second device (1511) was

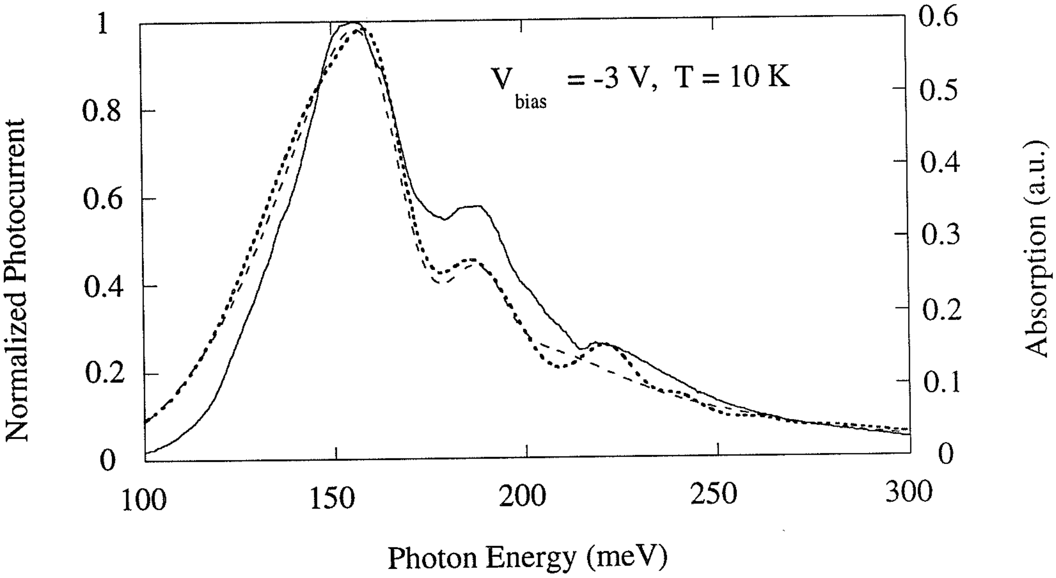

Figure 4.4: The experimental photocurrent spectrum at $V_{bias} = -3V$ (solid line) and theoretical absorption spectrum (dashed line for one period and dotted line for two periods) of Sample 1510 at T = 10 K.

fabricated and tested. This device had the same well width and barrier height as Sample 1510, however, the barrier width was increased to 400 Å. This gave a zero bias Kronig-Penney miniband structure which was very different from that of Sample 1510, but as it can be seen in Figure 4.5(a), the experimental photocurrent spectrum has peaks consistent with the calculated absorption spectrum of one quantum well in the superlattice.

Since the electron wave constructive and destructive interferences over periods of the superlattice strongly depend on the applied field, one can deduce the actual applied electric field over the quantum wells from the position and the spacing of the photocurrent peaks. Figure 4.5(a) shows the theoretical absorption spectrum for an applied electric field of 12 kV/cm which is consistent with the experimental value of -2.7 V potential drop over 50 periods of the superlattice. When the bias is decreased to -3.8 V ( Figure 4.5(b)), the photocurrent peaks move (their separation increases by ~6 meV), the theoretical absorption spectrum which reproduces this result requires an electric field of 17 kV/cm. This is again consistent with a -3.8 V drop over 50 periods of superlattice.

The photocurrent spectrum of the Sample 1510 (200 Å barriers) showed a different behavior as a function of applied bias. It showed the same peak positions as shown in Figure 4.4 for all biases between -0.2 and -4.3 volts. This result is explained through the formation of electric field domains in the multiple quantum well region. In this device, because of thinner barriers, the coupling between quantum wells is stronger. It has been observed previously that the conservation of lateral momentum

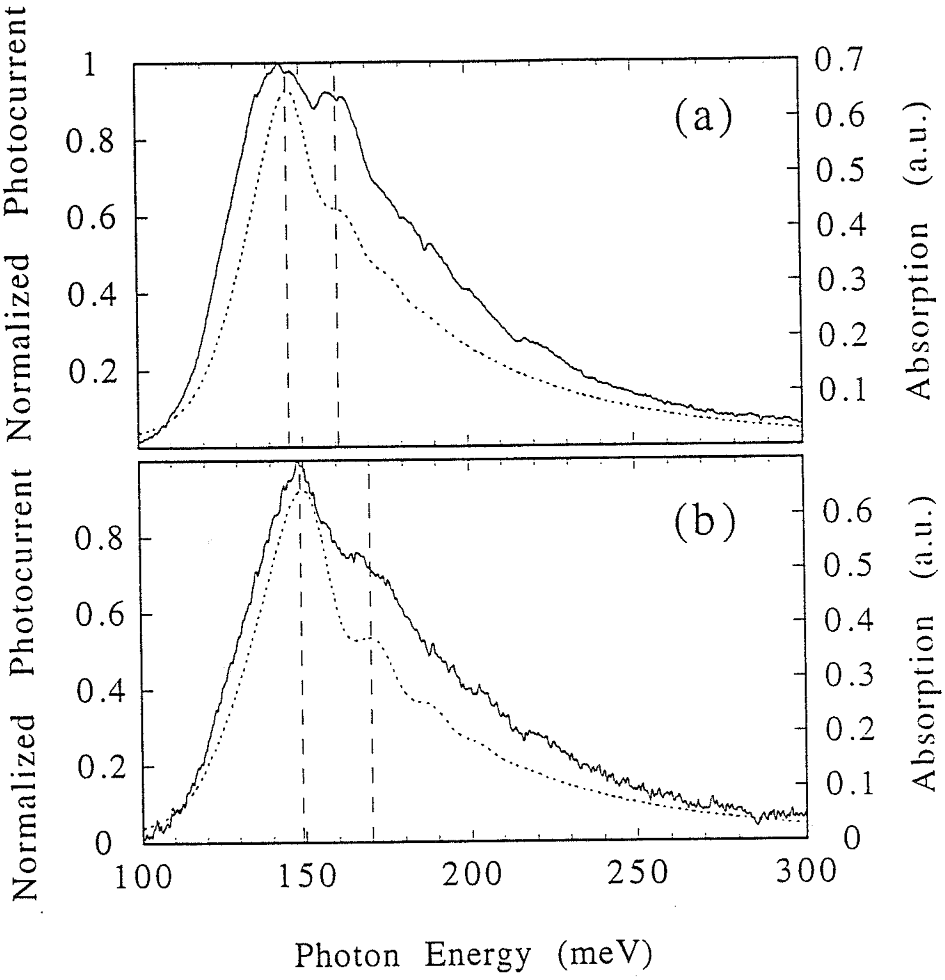

Figure 4.5: The experimental photocurrent spectra (solid line) and theoretical absorption spectra (dotted line) at different biases of Sample 1511 at T = 10 K. (a) $V_{bias} = -2.7V$; (b) $V_{bias} = -3.8V$.

in the tunneling process between wells induces current peaks whenever energy levels in adjacent wells are aligned [9,15,18]. This leads to an instability which causes formation of high and low field domains in the superlattice. In the high field domain, there is ground level-to-excited level sequential resonant tunneling. Whereas, in the low field domain, only ground level-to-ground level tunneling is possible. When the device is under infrared illumination, the light is absorbed in all the quantum wells but only those photoexcited carriers which are in a region with a high electric field have high probability of being swept out and contribute to the photocurrent. Those in low field regions have a high probability of being recaptured by their own wells, contributing negligibly to the photocurrent. The existence of electric field domains in the superlattice shows that electrons are coherent over about two superlattice periods (~400 Å). It is possible that the electron keeps phase coherence more than two superlattice periods.

It should be noticed that the electric field (~31 kV/cm) for which the theoretical results match the experimental ones does not correspond to an alignment between the ground state of one well with its neighboring well's resonant state. It is a little less than half of the aligned value. The ~31 kV/cm field for the high field domain in Sample 1510 seems to imply that the ground state of one well is aligned with the first resonance state of the *second* nearest neighbor.

Recently, Kwok et al. [18] explained the deviation of electric field in the high field domain from the resonant alignment through a phenomenological current continuity model. This phenomenological current continuity model can be explained through a schematic diagram as shown in Figure 4.6. The two peaks at $F_0$ and $F_1$ are due to $E_0 \rightarrow E_0, E_0 \rightarrow E_1$ subband resonant alignments, respectively. The electric field strength in the field domains is determined by current continuity through the superlattice. Because of this continuity condition, the electric field in the high field region is $F_c$, which is smaller than $F_1$. Further increase of external bias voltage will simply add more quantum wells to the high field region. When all the quantum wells are in the high field domain, a further increase in the external bias will increase the electrical field uniformly in the whole superlattice. If there are more bound states in each quantum well, similar picture can be described.

For the case of our single bound state quantum well device (1510), there are two ways to explain the subband alignment in the high field domain. One possibility is that the ground state of one well is (almost) aligned with the resonance state of its next neighboring well in the high field region, as shown in Figure 4.7. Another possibility is that the ground state is simply misaligned with the first resonance state of its immediate neighboring well because of current continuity as mentioned above (see Figure 4.8(a)). One should notice that the current continuity model does not rule out the first possibility. One way to check how the subband levels are aligned in the high field domain is by applying even higher external bias across the superlattice. If electrons are coherent over more than two superlattice periods, for bias larger than that required to align the ground state of each well to its second nearest neighbor, we could see the formation of a different high electric field domain in which the voltage drop per period correspond to the alignment of one well's ground state with

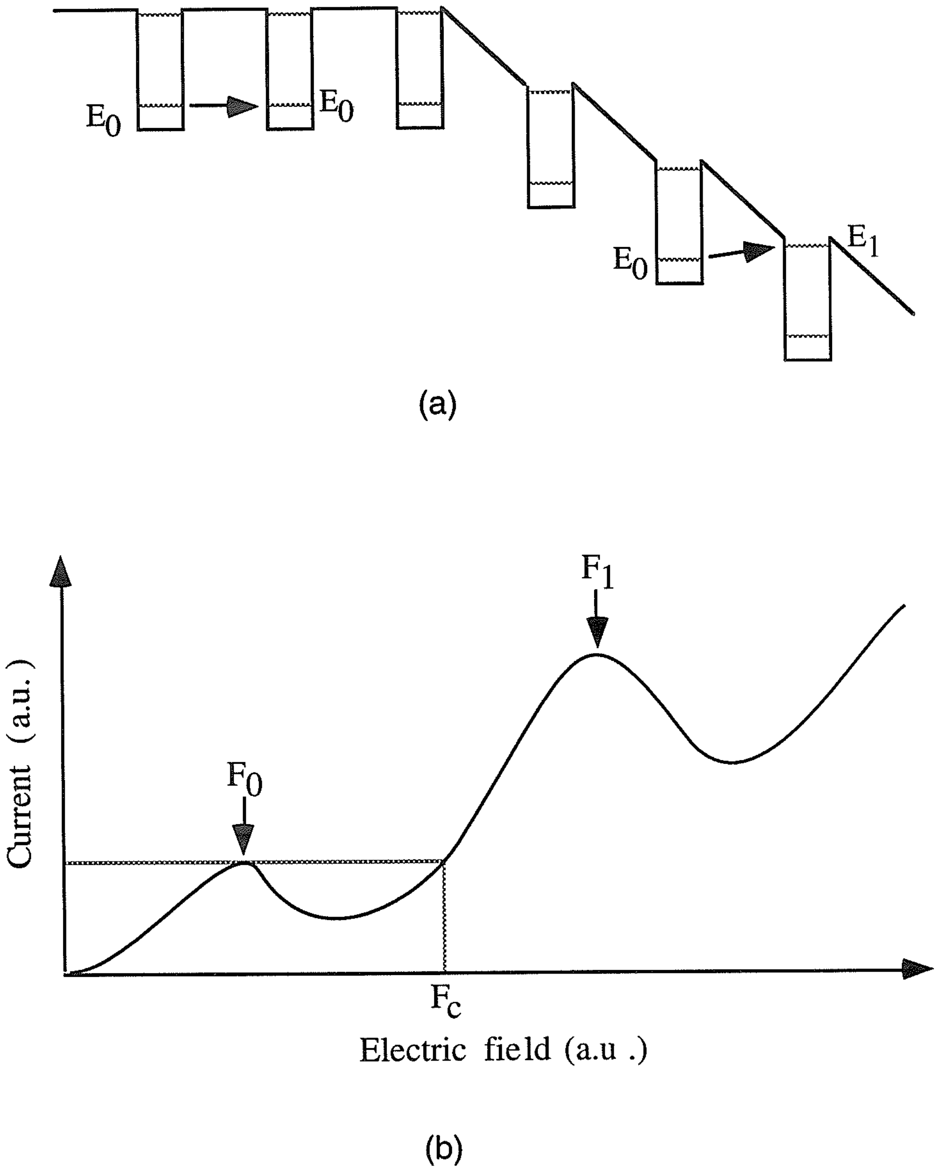

Figure 4.6: (a) Schematic drawing for a superlattice when electric field domains are formed. (b) Current versus field characteristics for a superlattice with single bound state in each well. The two peaks at $F_0, F_1$ corresponds to $E_0 \rightarrow E_0$ and $E_0 \rightarrow E_1$ resonant alignment, respectively. Notice that $F_c < F_1$, and the current is continuous only at $F_0$ and $F_c$.

its "neighboring" well's excited state (see Figure 4.8(c)).

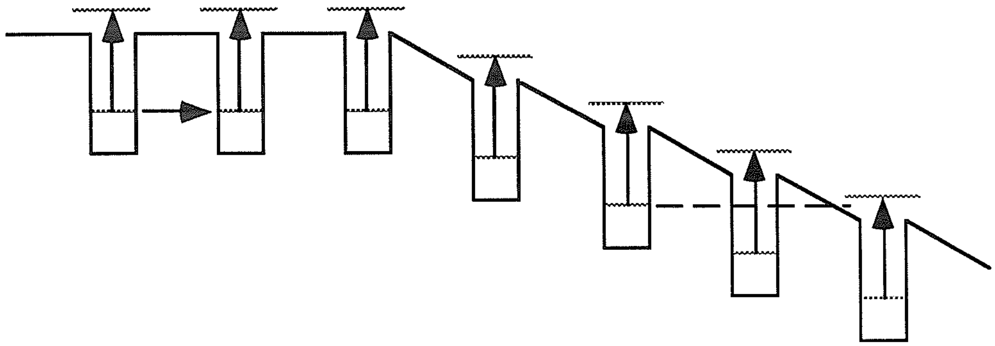

Figure 4.7: Sketch for the electric field distribution in the superlattice of Sample 1510.

At the highest bias that we could apply to these devices (−5 V), the experimental result, shown in Figure 4.9, shows peaks at ~128, 160, 200, and 230 meV. This could be explained either by a uniform voltage drop over the structure (see the dotted curve in Figure 4.9), or through the formation of a new high field domain in the structure. In the latter case, the broader peak at ~128 meV shows the low field domain contribution. Although we cannot conclusively determine that the ground state of one well is aligned with the first resonance state of the second nearest neighbor in the high field domain from this experiment, all the results are consistent with the fact that electrons remain coherent over two periods of the superlattice (for Sample 1510).

We estimated the electron coherence length in the above discussion, but the electron coherence length was not explicitly included. The electron coherence length can be included in the calculation of absorption spectrum through electron mean free path $L_e$ [19]. The fraction of the electrons that are coherent in the process of

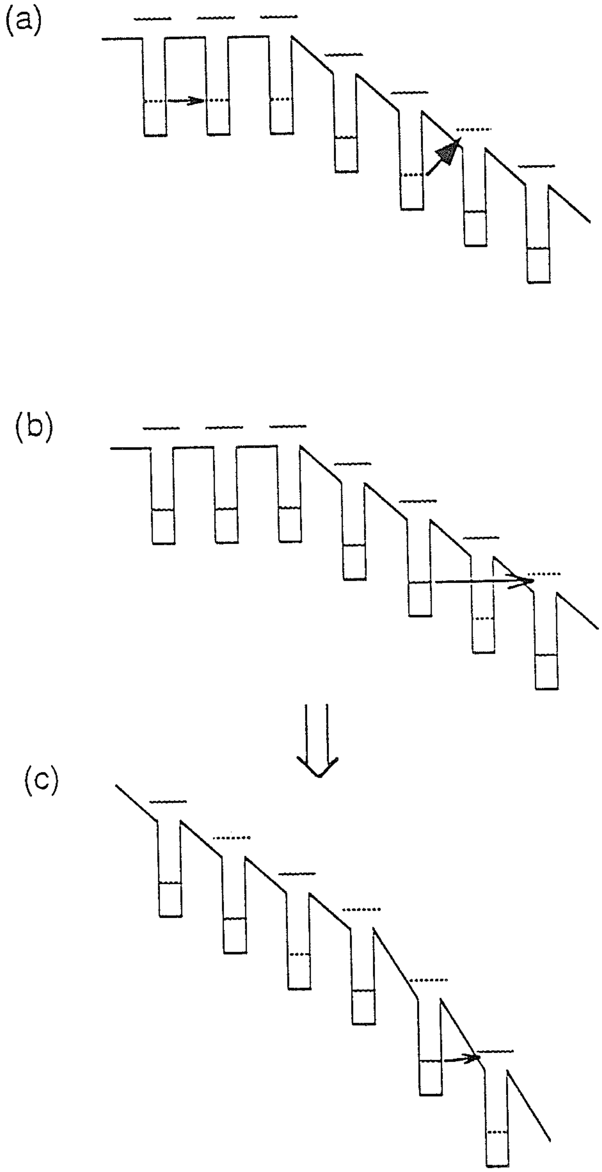

Figure 4.8: Sketch of possible electric field distribution in sample 1510.

photon absorption over a distance x in the superlattice is equal to $\kappa \cdot e^{-x/L_e}$, where $\kappa = 1/(\sum_{x=x_{min}}^{x_{max}} e^{-x/L_e})$ is a normalization constant, and the corresponding absorption is represented by $\alpha(x)$. Thus, the overall absorption is given by

$$\alpha = \sum_x \kappa e^{-x/L_e} \alpha(x). \tag{4.2}$$

This calculation also shows that the average electron coherence length is about 400 Å, in agreement with the above estimation. Although this calculation cannot give an upper limit to the electron coherence length, the upper limit is estimated to be less than 800 Å because of the fact that there are no electric field domains in Sample 1511.

Another signature of electric field domain formation in the sample is the oscillatory behavior in the I-V characteristics which reflects more quantum wells entering the high field domain region as the bias is increased [9,15,16]. In analogy to the Fabry-Perot interferometer, the larger the mirror reflectivity of the cavity, the narrower a Fabry-Perot mode. Similarly, the larger the barrier width in multiple quantum well structure, the weaker the coupling strength between neighboring wells and the more strict the requirement for energy level alignment (ground state in alignment with excited state under external bias). When the coupling between neighboring wells is too weak, there will be no different level alignment in the superlattice and thereby the device will show smooth I-V curve. As expected, Sample 1511 did not show any oscillations in the I-V characteristics, but there were 48 negative differential oscillations in the differential conductance-voltage curve for Sample 1510 (see the inset in Figure 4.9). This number is close to the number of quantum wells in the structure (i.e. 50). The very irregular period of these oscillations (75 ± 40mV), could originate from the fact that for this bound-to-continuum detector, the excited levels are a series of closely spaced states above the barrier. But the mean separation of these oscillations is close to half of the spacing in volts between the ground state and the first resonance state, and this is consistent with the electric field value estimated by fitting the photocurrent spectra.

Figure 4.10 shows the sweep-up and the sweep-down measurements of the I-V characteristics, which supports the multi-stability observation of Reference [20], and is an indication of the complexity of the growth of electric field domains in the device [21].

To check the statements about electric field domain formation in the superlattice, a second sample (Sample 1560) with exactly the same quantum well parameters as Sample 1510 but with half of the number of periods was grown and analyzed. It showed similar photocurrent spectra but the G-V characteristics had 23 to 24 negative differential oscillations. This is consistent with the smaller number of quantum wells in the device and supports the sequential resonant tunneling theory. Figure 4.11 shows the differential conductance of Sample 1560 as a function of voltage.

The importance of the end well barrier thickness for resonant tunneling was emphasized in Reference [22], where it was discussed that the transmission coefficient at the two end well barriers was several orders of magnitudes smaller than the transmission coefficient for any other well barriers if all quantum well barriers had the same

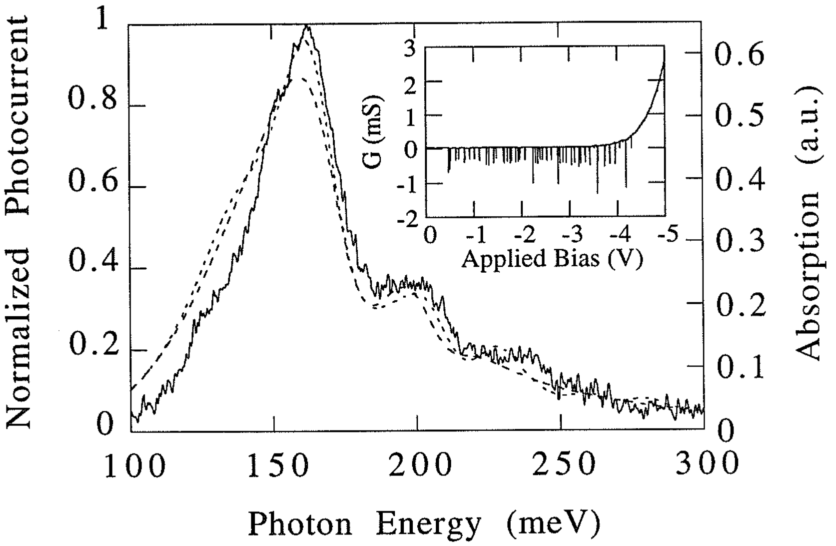

Figure 4.9: The experimental photocurrent spectrum of Sample 1510 at $V_{bias} = -5V$ (solid line) and theoretical absorption spectrum (dashed line for one period and dotted line for two periods) of Sample 1510 at T = 10 K. The inset is the differential conductance versus applied voltage at T = 10 K in dark. The number of negative differential oscillations for different devices processed out of the same wafer is between 45 to 49.

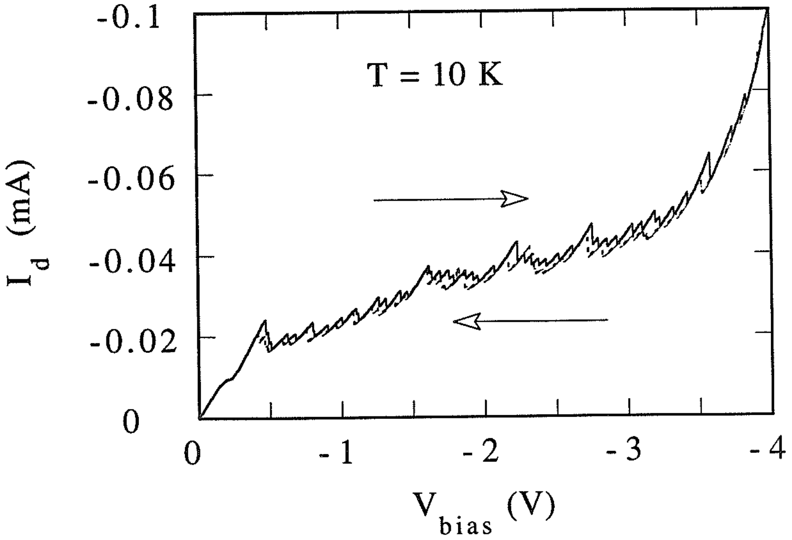

Figure 4.10: The dark current–voltage characteristics for increasing bias scan (thick line) and decreasing bias scan (thin line) at T = 10 K.

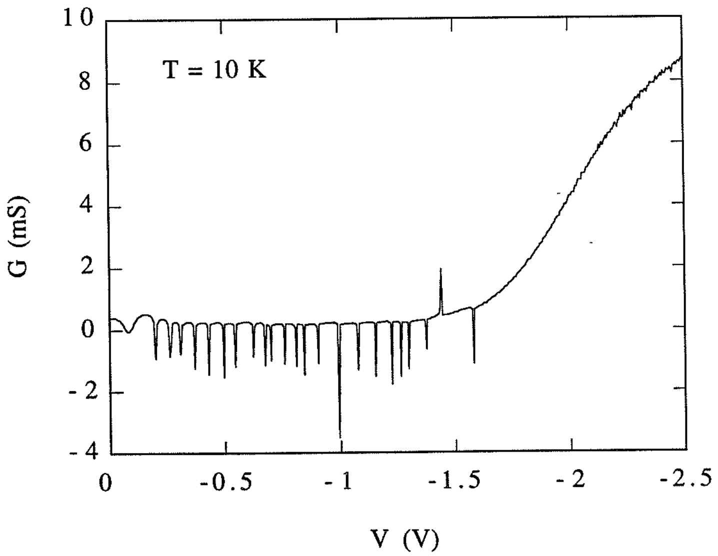

Figure 4.11: The differential conductance versus external applied bias for Sample 1560.

thickness. Because of the short coherence length of the electrons and the large barrier thickness in our samples, the considerations in Reference [22] are not important in the analysis of our results. At extremely low temperature (lower than 0.5 K), the consideration of Reference [22] might be important because it is possible that the electrons are coherent over a distance of several microns [23,24].

## 4.2 The effect of temperature on the electron coherence and electric field domain formation in MQW superlattices

Electron coherence length is the fundamental parameter which influences quantum interference effects and electric field domain formation in superlattices. Analyzing the photocurrent and the dark current of our devices, we can study the temperature dependence of the electron coherence length. As long as incoherent transport processes (such as thermionic emission or non-resonant tunneling) do not dominate the electric current, it should be possible to observe electric field domain effects at higher temperatures. Figure 4.12 shows the photocurrent spectra of Sample 1510 at different temperatures but at the same external bias (-2 V). The measured photocurrent spectrum at T = 50 K had a main peak at ~150 meV, corresponding to the transition from the ground state to the first resonant state. The small red shift of the peak position relative to that at T = 10 K can be explained by a reduction of the electric field strength in the high field domain. In this temperature range, the variation of the effective mass and the quantum well conduction band offset can be neglected [25]. The self-consistent simulation gives an electric field strength of ~26 kV/cm in the high field domain. One also notices the presence of a side peak at ~182 meV in the photocurrent spectrum at T = 50 K. This peak, being an indication of electron coherence over the quantum well structure [4], is less pronounced than the 10 K one. This suggests an increased contribution of incoherent processes to the photocurrent spectrum at higher temperatures. The reduction of electric field might also contribute to this observation (the resonance state is less localized for smaller electric field). The oscillations in the 50 K I-V characteristics show that the electric field domain formation in the device is still dominant.

One sees in Figure 4.12 that at a higher temperature of 70 K, the side peak at ~182 meV is almost invisible. This implies possible shortening of the electron coherence length and/or a reduction of electric field in the superlattice. In contrast to intersubband transitions between bound states, these bound-to-continuum transitions are very sensitive to both electron coherence length and the value of the internal electric field. This sensitivity originates from the extended nature of the excited states and from the electron wave interference effect over neighboring quantum wells.

Figure 4.13(a) shows the calculated absorption spectra at an electric field of 31 kV/cm, for two different values of electron coherence length. One notices the disappearance of side peaks for short coherence length. The theoretical absorption spectra at a different electric field of 16.6 kV/cm, are shown in Figure 4.13(b). It is apparent

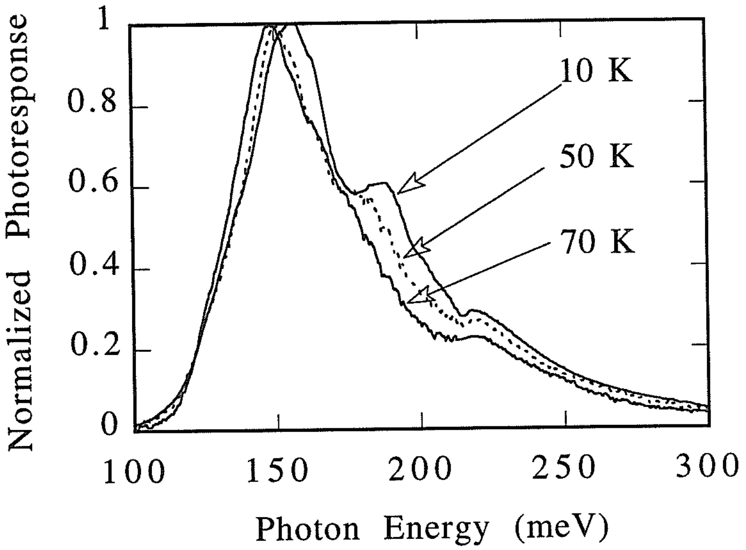

Figure 4.12: Experimental photocurrent spectra for the same bias and different temperatures.

that the side peak is very weak for low electric fields whatever the electron coherence length is.

To see how these two effects (a change in the electron coherence length or a change in the internal electric field) are contributing to the high temperature photocurrent spectra, the I-V characteristics at 70 K (Figure 4.14) were examined. The I-V characteristics does not show any appreciable oscillations. Since the current is dominated by non-resonant tunneling or thermally assisted processes, there is no sequential resonant tunneling induced electric field domain formation in this device. Thus, the disappearance of the auxiliary peak at 70 K, can be explained by assuming an electron coherence length less than 240 Å and/or a lower "*uniform*" electric field in the

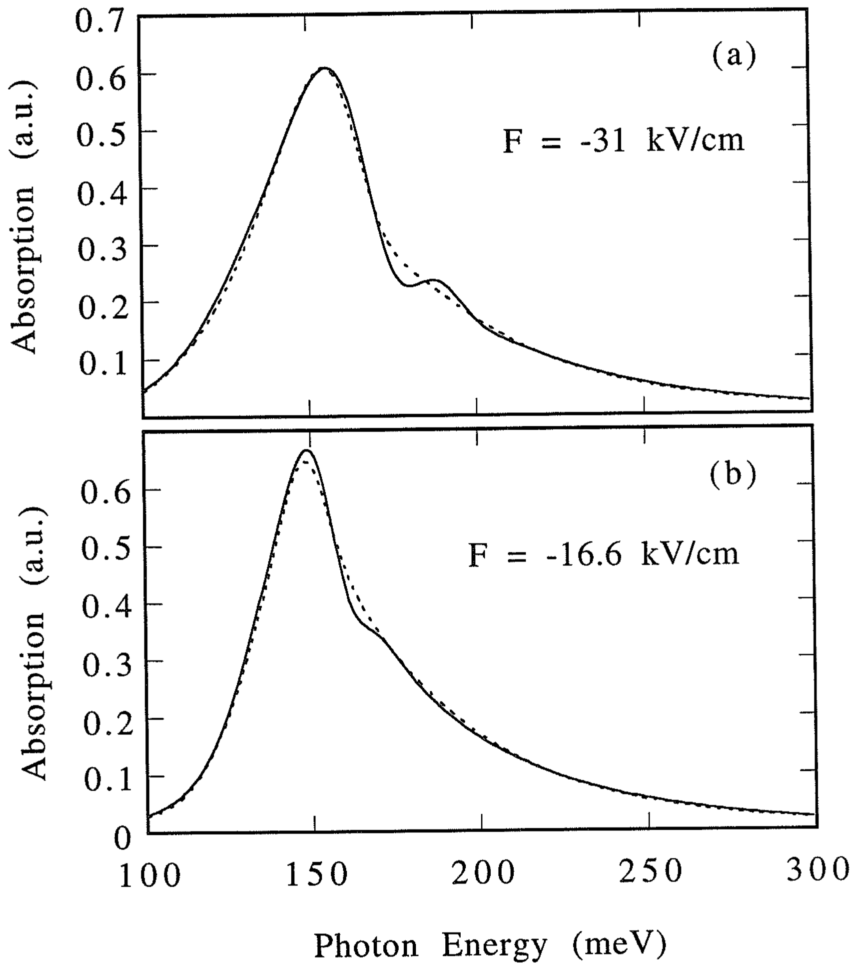

Figure 4.13: The overall absorption spectra assuming different electron coherence length (solid line: $L_e = 400$ Å, dot line: $L_e < 240$ Å), and different electric fields (a) F = 31 kV/cm, (b) F = 16.6 kV/cm.

superlattice. Reference [26] discusses the non-uniformity of electric field distribution near the edge of multiple quantum wells due to the fact that the three-dimensional cathode has to provide large two-dimensional current in the superlattice. Because of the large number of quantum wells and the high dopings in our structure, we neglected these edge effects.

It is interesting to note that the peak positions in the photocurrent spectra at 70 K have a voltage dependence in contrast to the low temperature peaks. This is consistent with the fact that no electric field domains exist in the device. One can see a blue shift of ~1.3 meV, when increasing the bias from −2 V to −3 V.

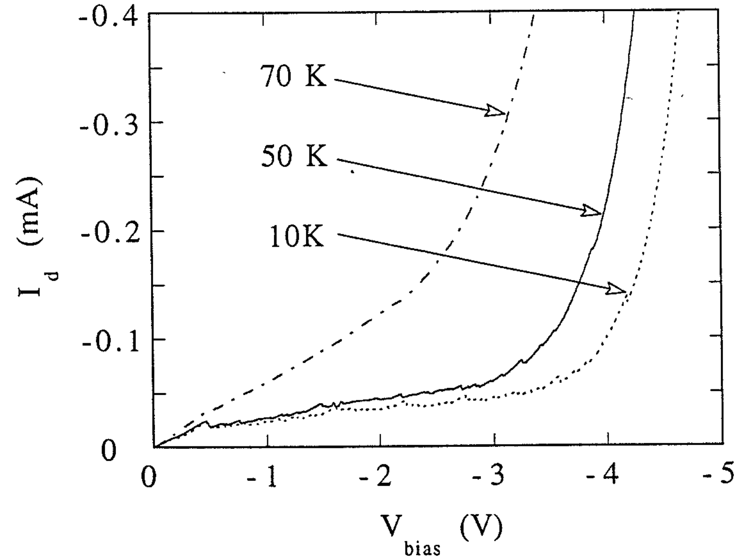

Figure 4.14: The I-V characteristics of Sample 1510 at different temperatures.

Another interesting optical experiment to study the electric field domain formation can be performed using the Stark effect. We can design a quantum well structure having both Stark effect and electric field domain formation. An example structure is shown in Figure 4.15. As mentioned before, there will be two regions with different electric fields in the superlattice (corresponding to low and high field domains) under external bias. Large Stark effect is preferred in this case in order to distinguish different absorption contributions from different field regions. Since the intersubband transition energies depend on the electric fields in the superlattice, we will expect extra absorption peak(s), as sketched in Figure 4.16. The peak positions are stationary with varying external bias, instead of a continuous absorption peak shift and no extra peak(s) in the case of no field domain formation. Notice that the relative strength of the peaks will change with different external biases, corresponding to various sizes of high and low electric field domains.

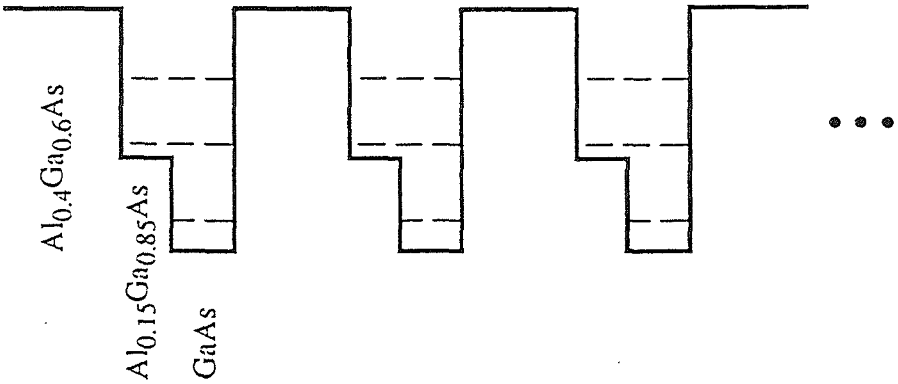

Figure 4.15: An example step quantum well structure used to study electric field domain formation: barrier: $Al_{0.4}Ga_{0.6}As$; step barrier: $Al_{0.15}Ga_{0.85}As$, 54 Å; well: GaAs, 59 Å.

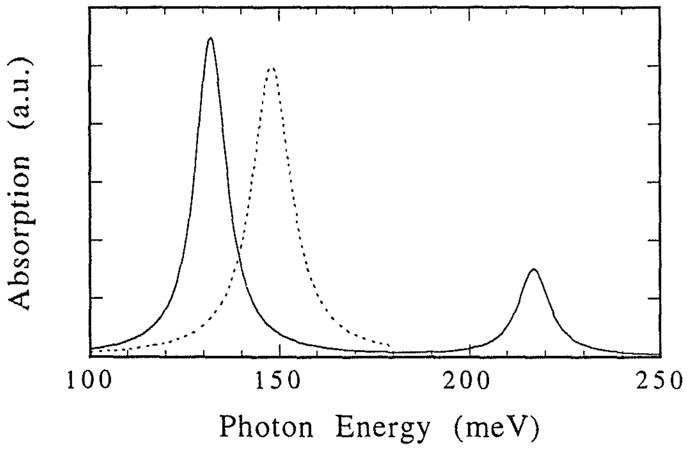

Figure 4.16: Absorption spectrum for the structure in Figure 4.15 when there are electric field domains in the superlattice. The relative strength of the peaks depends on the size of the high and low field domains.

## 4.3 Conclusion

We have presented a new observation of the quantum interference effect in the photocurrent spectrum of multiple quantum well structures. We estimated the coherence length of the electrons and analyzed the sequential resonant tunneling induced electric field domain formation by comparing the theoretical calculation with experimental results. A large energy level misalignment between two neighboring wells in the high field region was observed. The effect of temperature on the resonant tunneling and electric field domain formation was analyzed. Evidence for the domination of incoherent transport mechanisms at higher temperatures was presented. Electron coherence length shortening and/or reduced electric field in the superlattice are the likely cause of the disappearance of the auxiliary peaks in the photocurrent spectra at high temperatures.

# References

[1] D. Gershoni, J. Oiknine-Schlesinger, E. Ehrenfreund, and D. Ritter, "Minibands in the continuum of multi- quantum-well superlattices," Phys. Rev. Lett., vol. 71, no. 18, pp. 2975-2978, 1993.

[2] J. Faist, F. Capasso, A. L. Hutchinson, L. Pfeiffer, and K. W. West, "Suppression of optical-absorption by electric-field-induced quantum interference in coupled potential wells," Phys. Rev. Lett., vol. 71, no. 21, pp. 3573-3576, 1993.

[3] B. F. Levine, "Quantum-well infrared photodetectors," J. Appl. Phys., vol. 74, no. 8, pp. R1-R81, 1993 and the references there in.

[4] Y. Xu, A. Shakouri, and A. Yariv, "Quantum interference effect and electric-field domain formation in quantum-well infrared photodetectors," Appl. Phys. Lett., vol. 66, no. 24, pp. 3307-3309,1995.

[5] Y. Xu, A. Shakouri, and A. Yariv, "The effect of temperature on the resonant tunneling and electric field domain formation in multiple quantum well superlattices," submitted.

[6] J. B. Gunn, "Microwave oscillation of current in III-V semiconductors," Solid. State Commun., vol. 1, no. 4, pp. 88-91, 1963; "Instabilities of current in III-V semiconductors," IBM J. Res. Dev., vol. 8, no. 2, pp. 141-159, 1964.

[7] H. Kroemer, "Theory of Gunn effect," Proc. IEEE, vol. 52, p. 1736, 1964.

[8] L. Esaki and L. L. Chang, "New transport phenomenon in a semiconductor superlattice," Phys. Rev. Lett., vol. 33, no. 8, pp. 495-498, 1974.

[9] K. K. Choi, B. F. Levine, R. J. Malik, J. Walker, and C. G. Bethea, "Periodic negative conductance by sequential resonant tunneling through an expanding high- field superlattice domain," Phys. Rev. B, vol. 35, no. 8, pp. 4172-4175, 1987.

[10] W. L. Bloss, "Effects of Hartree, exchange, and correlation- energy on intersubband transitions," J. Appl. Phys., vol. 66, no. 8, pp. 3639-3642, 1989.

[11] D. F. Nelson, R. C. Miller, and D. A. Kleinmann, "Band nonparabolicity effects in semiconductor quantum wells," Phys. Rev. B, vol. 35, no. 14, pp. 7770-7773, 1987.

[12] Z. Ikonic, V. Milanovic, and D. Tjapkin, "Bound-free intraband absorption in GaAs-Al$_x$Ga$_{1-x}$As semiconductor quantum wells," Appl. Phys. Lett., vol. 54, no. 3, pp. 247-249, 1989.

[13] M. Murakami, "Development of Ohmic contact materials for GaAs integrated circuits," Materials Science Reports, vol. 5, pp. 273-317, 1990.

[14] F. Luc, E. Rosencher, and Ph. Bois, "Intersubband optical transients in multi-quantum-well structures," Appl. Phys. Lett., vol. 62, no. 20, pp. 2542-2544, 1993.

[15] R. F. Kazarinov and R. A. Suris, "Electric and electromagnetic properties of semiconductors with a superlattice," Sov. Phys. Semicond., vol. 6, p. 120 1972.

[16] F. Capasso, K. Mohammed, and A. Y. Cho, "Sequential resonant tunneling through a multiquantum well superlattice," Appl. Phys. Lett., vol. 48, no. 7, pp. 478-480, 1986.

[17] A. Shakouri, I. Grave, Y. Xu, and A. Yariv, "Control of electric-field domain formation in multiquantum-well structures," Appl. Phys. Lett., vol. 63, no. 8, pp. 1101-1103, 1993.

[18] S. H. Kwok, R. Merlin, H. T. Grahn, and K. Ploog, "Electric-field domains in semiconductor superlattices - resonant and nonresonant tunneling," Phys. Rev. B, vol. 50, no. 3, pp. 2007-2010, 1994.

[19] F. Beltram, F. Capasso, D. L. Sivco, A. L. Hutchinson, S.-N. G. Chu, and A. Y. Cho, "Scattering-controlled transmission resonances and negative differential conductance by field-induced localization in superlattices," Phys. Rev. Lett., vol. 64, no. 26, pp. 3167-3170, 1990.

[20] J. Kastrup, H. T. grahn, K. Ploog, F. Prengel, A. Wacker, and E. Scholl, "Multi-stability of the current-voltage characteristics in doped GaAs-AlAs superlattice," Appl. Phys. Lett., vol. 65, no. 14, pp. 1808-1810, 1994.

[21] D. Miller and B. Laikhtman, "Theory of high-field-domain structures in superlattices," Phys. Rev. B, vol. 50, no. 24, pp. 18426-18435, 1994.

[22] L. V. Iogansen, "Errors in papers on resonant electron tunneling in finite superlattices," Sov. Tech. Phys. Lett., vol. 13, no. 9, pp. 478-479, 1987.

[23] R. S. Prasad, T. J. Thornton, A. Matsumura, J. M. Fernandez, and D. Williams, "Quantum interference in the n-channel of a Si:SiGe quantum well," Semicond. Sci. Tech., vol. 10, no. 8, pp. 1084-1088, 1995.

[24] G. Fasol and H. Sakaki, "Effects of electron-electron scattering on quantum wave devices," Sol. State Commun., vol. 84, no. 1-2, pp. 77-80, 1992.

[25] J. S. Blakemore, "Semiconducting and other major properties of gallium arsenide," J. Appl. Phys., vol. 53, pp. R123-R181, 1982.

[26] L. Thibaudeau, P. Bois, and J. Y. Duboz, "Self-consistent model for quantum-well infrared photodetectors," J. Appl. Phys., vol. 79, no. 1, pp. 446-454, 1996.

[27] H. C. Liu, J. M. Liu, J. R. Thompson, Z. R. Wasilewski, M. Buchanan, and J. G. Simmons, "Multicolor voltage tunable quantum-well infrared photodetector," IEEE Trans. Electron. Devices, vol. 40, no. 11, pp. 2142-2142, 1993.

# Chapter 5

# Intersubband modulation and direct measurement of population-induced broadening of quantum well intersubband transitions

In the single band model, also known as the parabolic effective mass model, intersubband transitions in quantum wells are discrete. In practice, electron-electron interaction, quantum well width non-uniformity, electron interactions with rough interfaces, impurities, and optical and acoustic phonons contribute to the experimentally observed linewidth of intersubband transition in quantum wells [1,2,3,4,5]. Various broadening mechanisms can also be influenced by the applied electric field. Recently, there has been controversy over the direct contribution of electron population to this broadening. Bandara et al. [6,7] predicted that the dependence of the exchange interaction on the in-plane momentum ($k_{//}$) could contribute substantially to the experimentally observed linewidths. Zaluzny [8], on the other hand, claimed that the $k_{//}$ dependence is offset by the depolarization and exciton-like many-body effects, and the net result is that the transition linewidth is almost a constant as a function of population. This chapter describes a method to measure directly the population dependence of intersubband transition linewidth, based on the charge transfer between two coupled quantum wells [9]. The application of this method to a monolithically integrated intersubband modulator and detector is also investigated [12,13].

## 5.1 Superlattice structure

To measure the linewidth change for different electron populations in a quantum well, we might think of growing many samples with the same quantum well parameters except using different doping densities and measuring the absorption spectra for all samples. But an assumption inherent in this method is that the donor contribution to the measured linewidth is negligible or independent of different donor densities. Since we cannot justify this assumption in the first place, we cannot make any conclusions about the linewidth change for different electron populations and therefore cannot use this method .

Our solution to the above problem is to use an asymmetric coupled double quantum well (ACDQW) structure as shown schematically in Figure 5.1. We use one well as an electron reservoir and change the population in either well by applying an external bias or changing temperature.

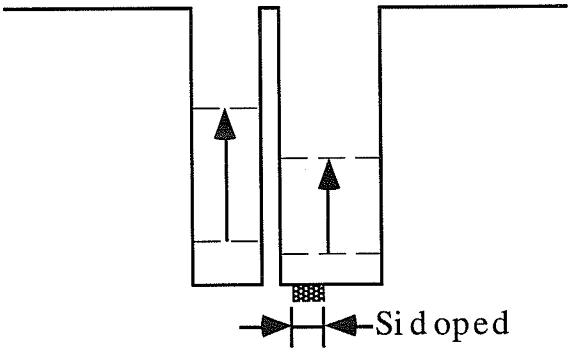

Figure 5.1: A schematic drawing of an asymmetric coupled double quantum wells.

The superlattice structure used in the experiment consisted of 50 periods of ACDQWs. A QWIP was monolithically integrated with the ACDQW superlattice to measure the low temperature absorption spectra. A change of the population in either of the ACDQWs will change the absorption spectrum and this can be directly measured with the monolithically integrated detector. The ACDQWs and the QWIP structures, shown in Figure 5.2, were grown by molecular beam epitaxy on a (100) semi-insulating GaAs substrate. The ACDQWs consisted of an undoped 90 Å-thick GaAs narrow well, an undoped 30 Å-thick $Al_{0.4}Ga_{0.6}As$ barrier, and a selectively doped 108 Å-thick GaAs wide well. The wide well was nominally Si doped to $2 \times 10^{18}$ $cm^{-3}$ from 5 Å to 45 Å away from the barrier. The periods were separated by 422

Å of undoped $Al_{0.4}Ga_{0.6}As$ layers. This structure was designed to provide the largest possible charge transfer between the narrow well and the wide well with external applied bias. The absorption spectrum of the monolithically integrated QWIP was designed to overlap with that of the narrow well in the ACDQWs, while the wide well in the ACDQWs had an absorption peak near the tail of the QWIP photoresponse spectrum. The QWIP was separated from the ACDQW structure by a 0.6 $\mu$m $n^+-$GaAs and a 0.2 $\mu$m GaAs buffer layer. The QWIP consisted of 15 periods of 65 Å-thick Si-doped GaAs wells with nominal doping density of $1.1 \times 10^{12}$ cm$^{-2}$ and 440 Å-thick $Al_{0.18}Ga_{0.82}As$ barriers.

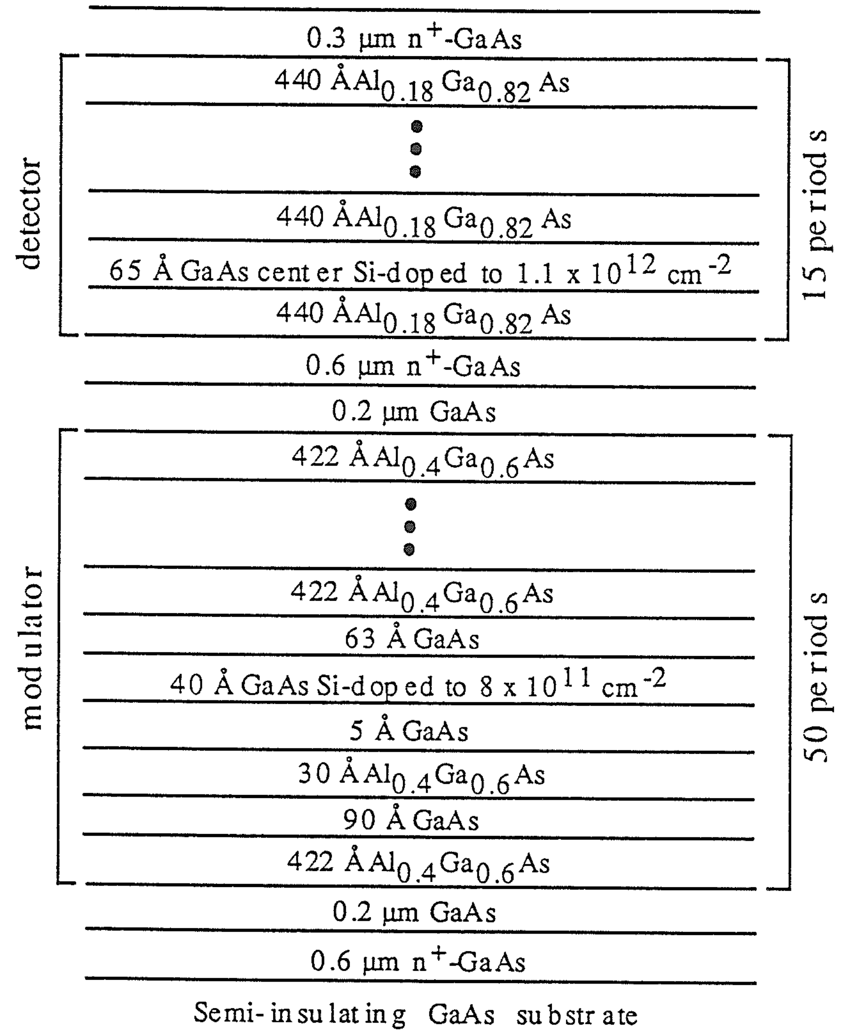

Figure 5.2: The ACDQW superlattice and the QWIP growth sequence.

## 5.2 Measurement of absorption spectra at room temperature

The room temperature absorption spectrum was done using the 45° multi-pass geometry [11]. Shown in Figure 5.3 is the absorption spectrum for the photodetector and the modulator. By etching away the photodetector layer, the absorption spectrum of the modulator was measured. From these two measurements, the absorption spectrum of the photodetector was calculated. It can be seen that the absorption peak of the narrow well in the ACDQW is very close to the QWIP one.

## 5.3 Measurement of population-induced broadening in intersubband transitions

As mentioned above, the absorption measurement at low temperatures was carried out using the monolithic quantum well infrared photodetector directly integrated on the asymmetric coupled quantum well superlattice. Figure 5.4 shows the sketch of a processed device.

The absorption linewidth measurements for different external biases on the ACDQW structure were made at 10 K with constant bias on the QWIP. As shown in Figure 5.5(a), the integrated absorbance for the narrow well increases almost linearly with the application of external bias. This corresponds to the transfer of population from the wide well to the narrow well. From the measured integrated absorbance and the

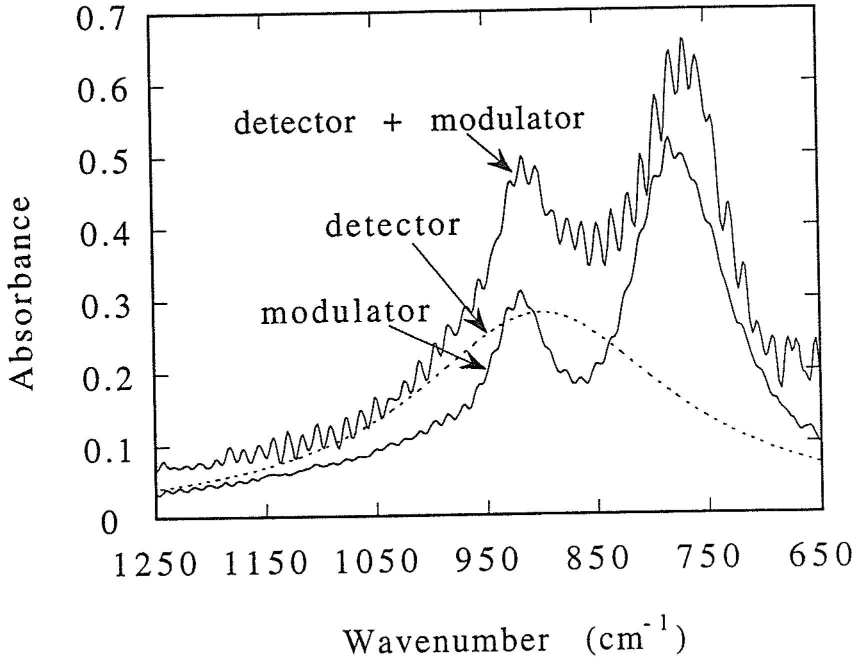

Figure 5.3: The absorption spectra at room temperature.

ACDQW parameters, the population in the narrow well was calculated. The absorption linewidth, which is the full width half maximum (FWHM), versus external bias is shown in Figure 5.5(b). At zero bias, the population in the narrow well was about $0.46 \times 10^{11}$ cm$^{-2}$ and the FWHM was about 3.75 meV. As it is clearly shown in Figure 5.5(b), the broadening increases with external bias. The maximum population transferred to the narrow well was about $6 \times 10^{11}$ cm$^{-2}$.

Figure 5.6 shows the linewidth as a function of the population in the narrow well with experimental data re-plotted from Figure 5.5. It also shows a theoretical plot of

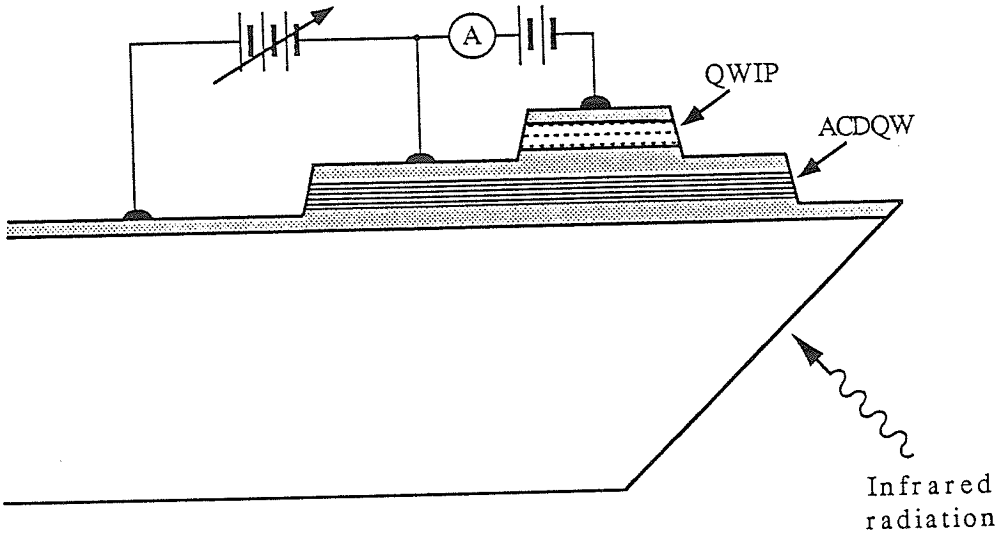

Figure 5.4: Sketch of the integrated QWIP on the asymmetric coupled double quantum well superlattice.

the exchange interaction broadening using an expression in [7] and the contribution of single-particle energy band non-parabolicity [14]. In the calculation of exchange interaction k-dependence, the following expression has been used [7]

$$E_{exch}(k) = -\frac{q^2 k_F}{4\pi\epsilon} \int dx \int dx' g(\xi,\eta) |\phi_1(x')|^2 |\phi_1(x)|^2, \tag{5.1}$$

where $k_F = (2\pi N_{2D})^{1/2}$ is the Fermi level for the two-dimensional density $N_{2D}$. The dimensionless function $g(\xi,\eta)$ is given by

$$g(\xi,\eta) = \frac{1}{\pi}\int_0^\pi d\theta \frac{1 - e^{-\xi\left(\eta\cos\theta + \sqrt{1-\eta^2\sin^2\theta}\right)}}{\xi}, \tag{5.2}$$

where $\xi = k_F|x - x'|$ and $\eta = k/k_F$. Notice that Equation (5.2) can be simplified as

$$g(\xi,0) = \frac{1 - e^{-\xi}}{\xi}, \text{ for } k = 0, \text{ or } \eta = 0;$$

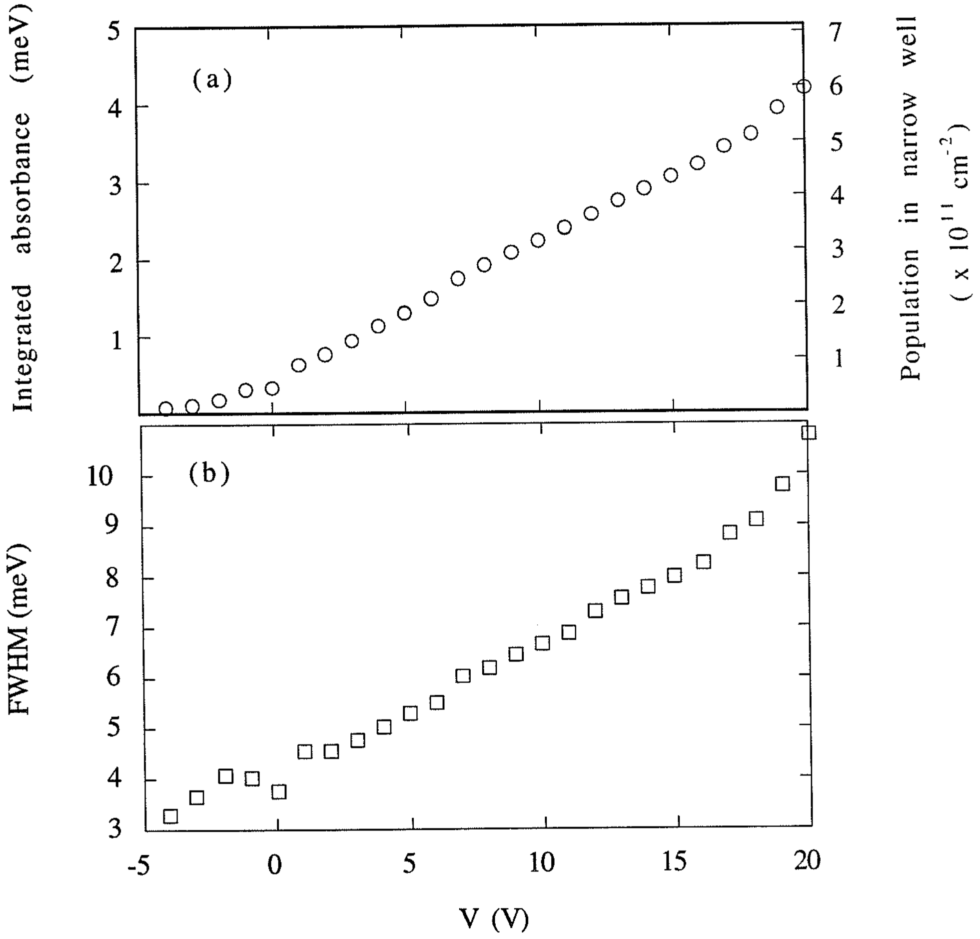

Figure 5.5: Absorption characteristics of the narrow well as a function of external bias at T = 10K. (a) The integrated absorbance and surface density versus external bias. (b) FWHM versus external bias.

$$g(\xi, 1) = \frac{1}{\pi} \int_0^{\pi/2} d\theta \frac{1 - e^{-2\xi \cos\theta}}{\xi}, \text{ for } k = k_F, \text{ or } \eta = 1.$$

The contribution from electron-electron dephasing broadening is expected to be small at these populations [1]. From the theoretical model [4], and from the bias-induced broadening of constant population wells, the bias-induced broadening due to interface roughness and impurity scattering was estimated to contribute less than 1 meV to the measured FWHM. The effective non-parabolicity created by the in-plane momentum dependence of the exchange interaction [7] is one of the main factors which could explain the measured broadening. It is evident from Figure 5.6 that the theoretical exchange interaction broadening increases with the population in the narrow well and is close to the experimental results. It should be noticed that the single-particle energy band non-parabolicity may also contribute to the linewidth [14] (at most up to ~4.5 meV at the highest bias) as shown in Figure 5.6, part of which will be compensated by depolarization and exciton effects. Because the exchange-interaction makes a large contribution to the broadening, we expect that the depolarization and exciton effects contribute by reducing the theoretical broadening [8]. But they will not change the situation drastically. Our experimental results show that the linewidth broadens as the electron population increases, instead of the theoretical constant broadening as a function of population, which was predicted in Reference [8]. For populations less than $1 \times 10^{11}$ cm$^{-2}$, the minimum linewidth is limited by other broadening mechanisms. When the bias is such that the ground states of the coupled wells are anti-crossing, at which point the population in the narrow well is about $4 \times 10^{11}$ cm$^{-2}$, it is hard to get a convergent solution from the self-consistent calculation because of the anti-crossing of the ground states. Near this anti-crossing bias, one might expect to see an increase in the broadening. This would be due to the increase in impurity scattering and in field-induced scattering at interfaces because the ground states are spread over both wells. Figure 5.5 shows that this broadening is not significant, and one does not see any appreciable peak in FWHM around the bias of 14 volts. The crossing of the ground states of the coupled wells is further supported by the red-shift of the absorption peak position at high biases. For larger populations near $6 \times 10^{11}$ cm$^{-2}$, external field-induced broadening may have some contribution [15].

As a further check on our results, the absorption spectra at different temperatures ($83 \sim 380$ K) were measured in multiple-pass geometry using 45° polished edge mirrors. No bias was applied so that the populations of both the narrow and wide quantum wells were a function of temperature only. From $N_{2D} = \int dE \rho_{2D} f(E)$, where $\rho_{2D}$ is the two-dimensional density of states and $f(E)$ is the Fermi function, we might think the populations of both wells in the ACDQW structure have similar temperature dependence since $\rho_{2D}$ is a constant. At a given doping density, changing temperature will redistribute electrons between the coupled quantum wells because of the ground state energy level difference and the change of this difference caused by many-body effects. This causes the different population temperature dependence for the coupled wells. The integrated absorbance and the FWHM as a function of temperature is plotted in Figure 5.7.

At room temperature, the population in the narrow well was about $1.79 \times 10^{11}$

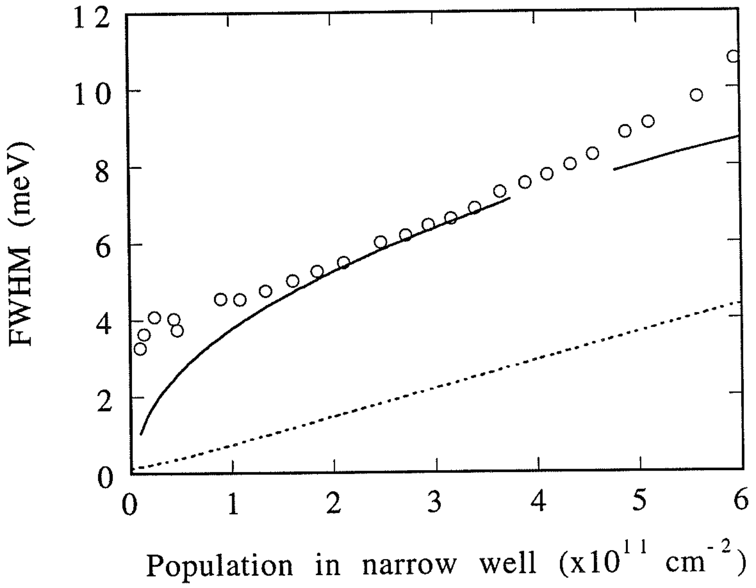

Figure 5.6: Experimental FWHM ( o ), theoretical exchange interaction broadening (solid line), and single-particle non-parabolicity broadening (dashed line) versus surface density.

cm$^{-2}$, which was 22.4% of the total population, and the corresponding broadening was $\Gamma \approx 6.6$ meV. The lowest temperature for this multiple pass absorption experiment is limited to 83 K in the experimental setup. It can be seen in Figure 5.7 that varying the temperature from 83 K to 380 K caused an increase of the linewidth of 5.5 meV (from 3.2 meV to 8.7 meV) in the narrow well. At the same time, the FWHM of the wide well increased by only 1.9 meV, from 9.3 meV to 11.2 meV. Apparently, the linewidth due to temperature effect is significant. As the temperature increased from 83 K to 380 K, the population-induced-broadening in the wide well, whose

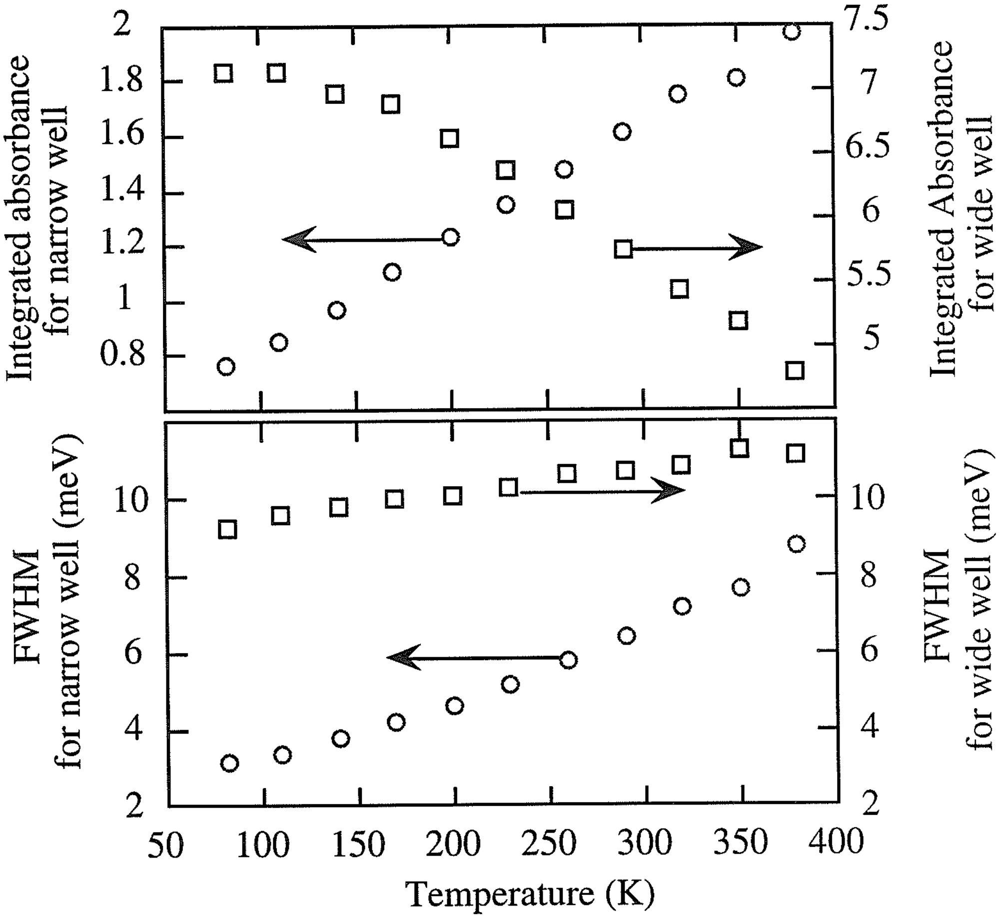

Figure 5.7: The integrated absorbance and the linewidth of the narrow well versus different temperatures.

population dropped, acted counter temperature induced increase in linewidth. In the narrow well, which gained population, population-induced-broadening assisted the linewidth increase due to the temperature effect. The many-body and single-particle non-parabolicity broadening temperature dependence are the possible causes of the increase of FWHM with increasing temperature for both wells. It should be noticed that the large difference of the FWHM between low and room temperatures (much larger than the typically measured value for constant well population) is consistent with the increase of population in the narrow well and with the thermal spread to higher momentum states.

Although the exact population may be material dependent, our experimental results show that population-induced broadening is very important in the spectral measurement of intersubband transitions in quantum wells. Even with the donors 5 Å away from the 30 Å-thick barrier in our experiment, a broadening of only 3.75 meV was achieved. Thus, the broadening may not be significantly decreased by separating the donors from the wells at the same electron population. Although donor position versus broadening was studied before [16], the effect of different populations in the quantum wells for different doping positions in the quantum well barriers in [16] was neglected.

## 5.4 Intersubband absorption modulation

In two-dimensional focal plane QWIP array applications, such as imaging, there is great interest in eliminating the dark current to avoid saturating the readout circuit and to increase the pixel integration time. Using a light chopper in front of the QWIPs, the photocurrent is an 'AC' signal, therefore, the DC dark current current can be filtered out by AC coupling the multiplexer [17]. This section describes the demonstration of an intersubband absorption modulator as an electronic light chopper. From Equation (2.7), we know that the intersubband transition absorption is proportional to the population in the quantum well.

$$\alpha(\hbar\omega) = \frac{\pi q^2}{\hbar n c \epsilon_0} N_{2D} |\mu_{ij}|^2 \hbar\omega \frac{\hbar/T_2}{(E_j - E_i - \hbar\omega)^2 + (\hbar/T_2)^2}. \tag{5.3}$$

If we can modulate the population in the quantum well, we can modulate the absorption. This can be realized using a ACDQW structure such as the one discussed in the above section because we can change the electron population in either one of the wells by changing the external bias.

We may also notice from Equation (5.3) that the absorption spectrum has a narrow peak. For a given incident infrared radiation (given wavelength), another way to modulate the absorption is by shifting the absorption spectrum peak position, as sketched in Figure 5.8. One way to achieve this is to use a specially designed quantum well sample to have a large Stark effect (e.g., a step quantum well structure). From the Kramer-Kronig relations [18], we know that there is a refractive index change due to this absorption spectrum shift, which has some applications in phase modulators.

However, it is undesirable for many high speed applications.

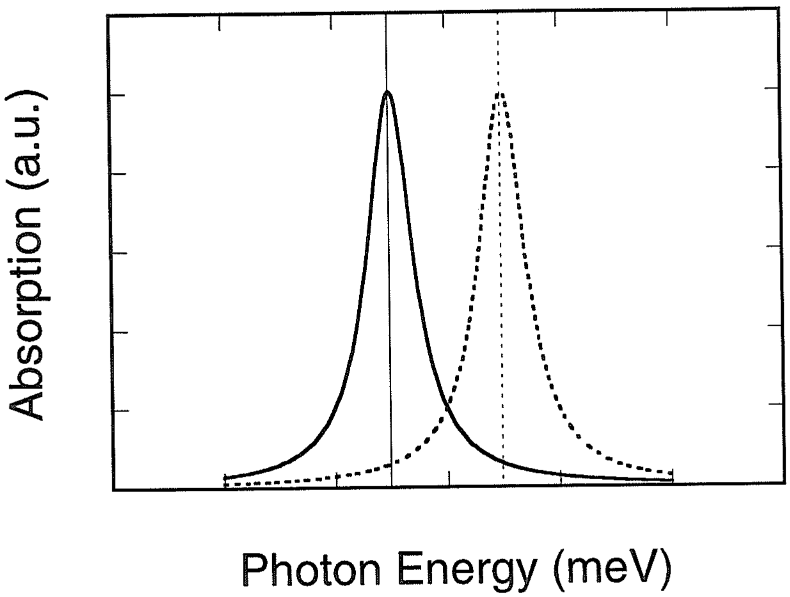

Figure 5.8: Sketch of shift absorption spectrum center frequency modulation.

Although a modulator based on Stark effect can be used for low speed applications such as chopper, we chose to use the ACDQW structure in a chopper. (Notice that the detector does not detect the signal phase change. A large Stark shift will cause the chopper to be open at different time for different wavelength, which limits the chopper high speed application.) From the detector photoresponse spectra for different modulator biases (see Figure 5.9), we found that a 40% modulation depth at 10.4 $\mu$m wavelength was achieved for +14 V bias we applied to the device discussed in the above section. A 45% modulation depth was obtained at a higher bias of +20 V. When very large negative bias was applied on the modulator, there were no electrons in the narrow wells. The modulator should be transparent for the incident light. The very small distortion of the −13 V detector photoresponse peak shown in Figure 5.9 is due to a very small amount of light scattered from adjacent unbiased device(s).

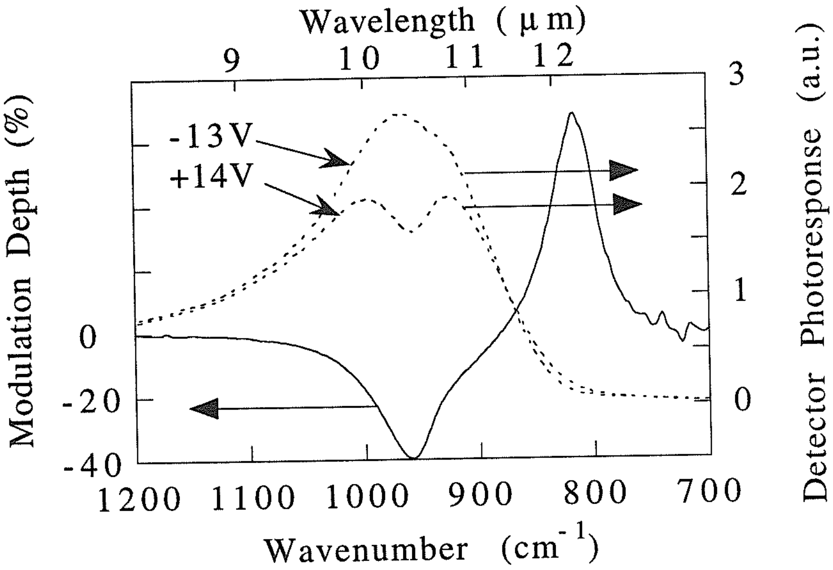

Figure 5.9: The modulation depth spectrum calculated from the detector photoresponse spectra while the bias on the detector was kept constant.

Shown in Figure 5.10 is the absorption spectrum peak position of the narrow well of the modulator at different biases. Apparently, the Stark shift is small (about 2 meV), which is good for modulator applications.

To increase the modulation depth, we could increase the number of periods of ACDQWs in the modulator. However, a better way might be utilizing both Stark effect and charge transfer to optimize the modulator quantum well structure because Stark effect is not a problem for chopper applications as mentioned above. An example

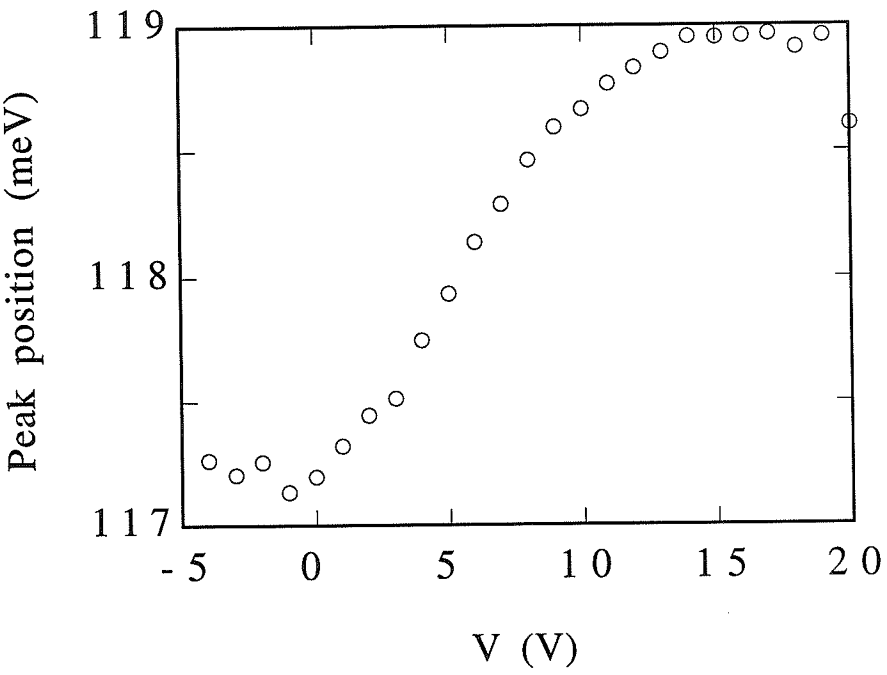

Figure 5.10: The absorption spectrum peak position versus external bias.

structure is sketched in Figure 5.11, where the intersubband transition in the step well is used for intersubband modulation, while the other simple well is used as electron reservoir.

We demonstrated the monolithically integrated device using 45° edge mirror to couple the incident light. Practically, it is always desirable to use vertically incident light coupling (i.e., the incident light is polarized in the quantum well plane). This can be realized by using a two-dimensional metallic grating or etched GaAs grating.

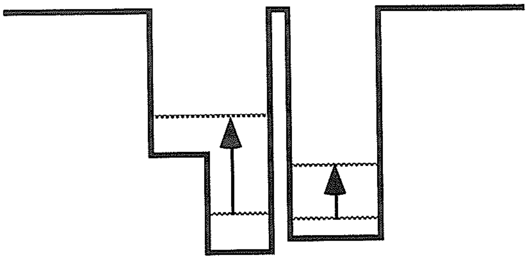

Figure 5.11: A modulator with a step well and a simple well. The intersubband transition in the step well is used for intersubband modulation. The simple well is used as electron reservoir.

## 5.5 Conclusion

We observed an increase of the intersubband absorption linewidth with increasing electron population using field-induced charge transfer and thermally-induced charge transfer in specially grown quantum well structure. This increase is attributed mainly to the subband filling. Many-body effects and single-particle band non-parabolicity are the likely causes. The field-induced charge transfer between asymmetric coupled quantum wells could be used in intersubband modulations. 45% modulation depth was demonstrated using a 50-period ACDQW superlattice.

# References

[1] P. Sotirelis, P. von Allmen, and K. Hess, "Electron intersubband relaxation in doped quantum-wells," Phys. Rev. B, vol. 47, no. 19, pp. 12744-12753, 1993.

[2] H. Sakaki, T. Noda, K. Hirakawa, M. Tanaka, and T. Matsusue, "Interface roughness scattering in GaAs/AlAs quantum wells," Appl. Phys. Lett., vol. 51, no. 23, pp. 1934-1936, 1987.

[3] W. T. Masselink, "Ionized-impurity scattering of quasi-two-dimensional quantum-confined carriers," Phys. Rev. Lett., vol. 66, no. 11, pp. 1513-1516, 1991.

[4] R. Ferreira and G. Bastard, "Evaluation of some scattering times for electrons in unbiased and biased single-quantum-well structures," Phys. Rev. B, vol. 40, no. 2, pp. 1074-1086, 1989.

[5] P. J. Price, "Two-dimensional electron transport in semiconductor layers. I. Phonon scattering," Ann. Phys., vol. 133, pp. 217-239, 1981.

[6] K. M. S. V. Bandara, D. D. Coon, Byungsung O, Y. F. Lin, and M. H. Francombe, "Exchange interactions in quantum well subbands," Appl. Phys. Lett., vol 53, no. 20, pp. 1931-1933, 1988.

[7] J. W. Choe, Byungsung O, K. M. S. V. Bandara, and D. D. Coon, "Spectral linewidths of quantum-well intersubband transitions," Superlattices and Microstructures, vol. 10, no. 1, pp. 1-4, 1991.

[8] M. Zaluzny, "On the intersubband absorption-line width in semiconductor quantum-wells," Solid State Comm., vol. 82, no. 7, pp. 565-567, 1992.

[9] Y. Xu, G. Almogy, J. O'Brien, A. Shakouri, W. Xu, R. A. Salvatore, and A. Yariv, "Direct measurement of population-induced broadening of quantum well intersubband transitions," accepted for publication in Appl. Phys. Lett.

[10] M. O. Manasreh, F. Szmulowicz, T. Vaughan, K. R. Evans, C. E. Stutz, and D. W. Fischer, "Intersubband infrared absorption in a GaAs/$\mathrm{Al_{0.3}Ga_{0.7}As}$ multiple quantum well," *NATO Advanced Research Workshop on Intersubband Transitions in Quantum Wells*, edited by E. Rosencher, B. Vinter, and B. Levine, vol. 288, pp. 287-297.

[11] see Chapter 4.

[12] Y. Xu, G. Almogy, A. Shakouri, and A. Yariv, "Monolithic integration of a quantum-well IR photodetector and modulator," CLEO'95, Baltimore, paper CThQ4.

[13] G. Almogy, Y. Xu, A. Tong, A. Shakouri, and A. Yariv, "Monolithic integration of quantum-well infrared photodetector and modulator," Appl. Phys. Lett., vol.68, no. 15, pp. 2088-2090, 1996.

[14] Z. Ikonic, V. Milanovic, and D. Tjapkin, "On the linewidth of intersubband transitions in GaAs-$Al_xGa_{1-x}As$ quantum wells in electric-field," Solid State Comm., vol. 72, no. 9, pp. 835-838, 1989.

[15] B. F. Levine, C. G. Bethea, K. K. Choi, J. Walker, and R. J. Malik, "Tunneling lifetime broadening of the quantum well intersubband photoconductivity spectrum," Appl. Phys. Lett., vol. 53, no. 3, pp. 231-233, 1988.

[16] E. B. Dupont, D. Delacourt, D. Papillon, J. P. Schnell, and M. Papuchon, "Influence of ionized impurities on the linewidth of intersubband transitions in GaAs/GaAlAs quantum-wells," Appl. Phys. Lett., vol. 60, no. 17, pp. 2121-2122, 1992.

[17] B. F. Levine, "Quantum-well infrared photodetectors," J. Appl. Phys., vol. 74, no. 8, section XVII, p. R70, 1993.

[18] A. Yariv, Quantum Electronics, New York: John Wiley and Sons, $3^{rd}$ edition, pp. 160-161, 1989.

# Appendix A

# Device processing for a quantum well photodetector

1. Strip off Indium on the backside of the MBE grown sample to get flat surface. Then, clean the sample using the standard cleaning and drying procedure (acetone + ultrasonic, methanol + ultrasonic, deionized-water rinse, and $N_2$ blow dry). This step is necessary for spinning photoresist on the sample at later processes.
2. Spin on photoresist S1400-31, soft-bake at 90°C for 30 minutes.
3. Direct contact exposure, develop in developer, followed by deionized-water rinse and blow dry.
4. Hard-bake the sample.
5. Etching GaAs/AlGaAs is generally done using $H_2SO_4 : H_2O_2 : H_2O = 1$

: 8 : 80. The etching depth is controlled by timing. (A test sample can be used to measure the etching rate.) This step is very important because the etching should be stopped in the middle of the bottom $n^+$-GaAs contact layer and the series connection resistance should be minimized (the bottom $n^+$-GaAs layer is the main contributor to the series resistance of the photodetector). If we use $R_c$ to represent the $n^+$-GaAs layer series connection resistance and use the following equivalent circuit,

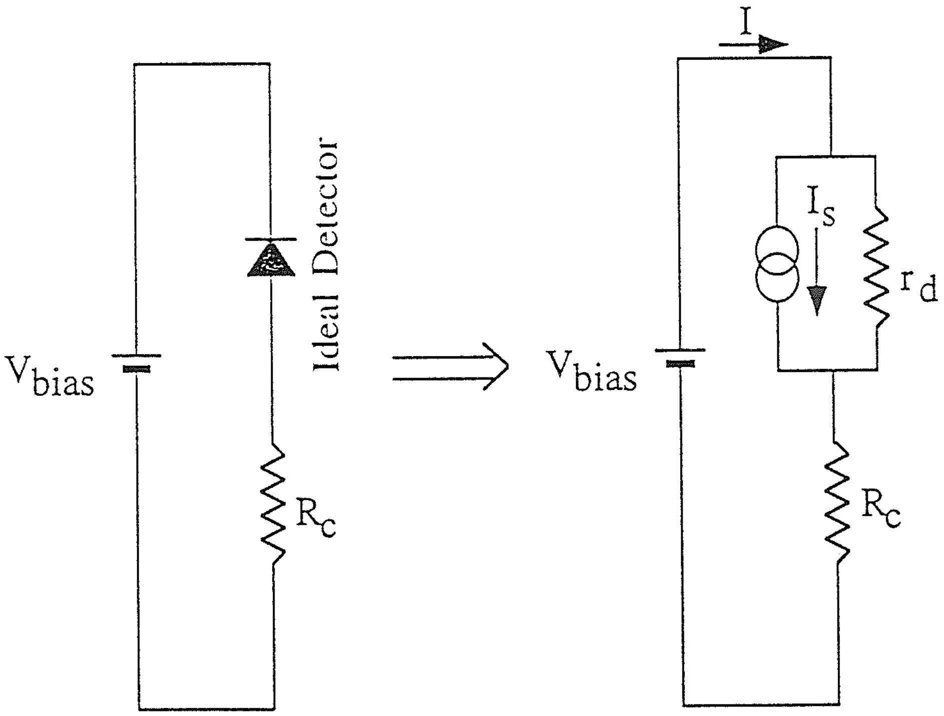

Figure A.1: Equivalent circuit for a processed photodetector.

we can get

$$I = \underbrace{I_s \cdot \frac{1}{1 + R_c/r_d}}_{signal} + \underbrace{\frac{V_{bias}}{r_d + R_c}}_{darkcurrent} .$$

So, the measured $I \approx I_s +$ (dark current) when $R_c << r_d$. $R_c$ is normally between 25 Ω to 100 Ω after the following annealing step.

Selective etchants such as succinic acid with ammonia, $H_2O_2$, and $H_2O$ can also be used for low Al concentration ($x < 0.4$ in $Al_xGa_{1-x}As$) devices and in this case, an additional stop-etch layer, such as a 30 Å-thick AlAs layer, is needed in the middle of the bottom $n^+-$ GaAs contact layer [2].

6. Metal contact pattern is formed using a liftoff procedure with positive photoresist. The photolithography procedure is similar to step (2), but the photoresist layer is thicker for the purpose of liftoff, and there is no hard-bake. The sample is further briefly cleaned in an $O_2$ plasma chamber. The contact metal for $n^+-$ GaAs is AuGe/Ni/Au. It is important to use the appropriate thickness of AuGe and Ni to obtain shallow metal diffusion depth into GaAs layer [1]. The Au thickness of 2000 Å is enough for wire bonding. The liftoff is done in acetone.
7. Anneal in $H_2$ atmosphere. Annealing time should be as brief as possible so that the metal diffusion depth into GaAs is smaller than the top $n^+-$ GaAs contact layer thickness and long enough to make the contact ohmic.
8. Evaporate AuGe/Au or Cr/Au on the backside of the sample as a mirror to avoid the bonding epoxy absorption in the infrared region.

9. Polish 45° edge mirror. (The finest power used to polish the mirror has the grain size of $\lambda_p/30 \sim \lambda_p/10$, where $\lambda_p$ is the vacuum peak intersubband transition wavelength.)

10. Package the processed sample onto a multiple pin IC-package (such as CPG08422) or a 6-pin Ortel mount.

11. Wire bond the devices. Notice that the etched mesa surface is only ~2 $\mu$m above the bottom contact and there is no insulating layer for passivation (actually, most passivation materials, such as $SiO_2$, are absorbing in the mid-infrared range). So, care must be taken.

# References

[1] M. Murakami, "Development of Ohmic contact materials for GaAs integrated circuits," Materials Science Reports, vol. 5, pp. 273-317, 1990.

[2] A. J. Tang, K. Sadra, and B. G. Streetman, "Selective etching of $Al_xGa_{1-x}As$ and $In(Al_xGa_{1-x})As$ alloys in succinic acid-hydrogen peroxide solutions," J. Electrochem. Soc., vol. 140, no. 5, pp. L82-L83, 1993.

# Appendix B

# Note on photocurrent measurement

The circuit shown in Figure B.1 has been used to measure the detector photoresponse spectrum of a detector. The resistor R is about 10Ω [1].

The resistance R should be much smaller than the differential resistance of the detector in order to be able to apply bias to the detector. On the other hand, since the photocurrent is generally very small, R should be as large as possible so that $V_o$ is larger than the noise generated in the wire itself, which is important for FTIR measurements without lock-in amplification.

The disadvantage of using the circuit shown in Figure B.1 can be seen from the following discussion. Assuming that the readout circuit is perfectly noiseless, we use a perfect capacitor to represent it. The above circuit is redrawn in Figure B.2.

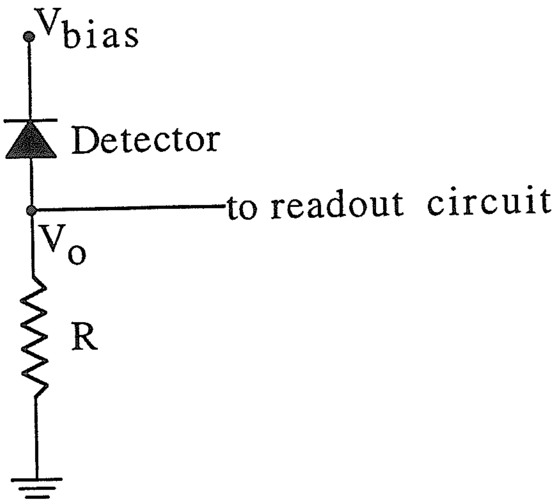

Figure B.1: Circuit using R to measure detector photoresponse.

The readout noise due to the thermal noise of R is

$$v_o^2 = \frac{1}{1 + (2\pi\nu RC)^2} \cdot 4kTR\Delta\nu.$$

Three ways to reduce the noise are:

(1) cooling R to low temperature;

(2) increasing R to infinity;

(3) decreasing the bandwidth $\Delta\nu$ using lock-in amplification, which is very effective, but not adopted in our experiment because it does not work with the Galaxy 2020 FTIR spectrometer.

The disadvantage of the first method is that it is not convenient when different temperature characteristics of the detector are needed (R will change with changing temperature, and the noise will change, too). To adopt the second method, a circuit shown in Figure B.3 is used. In this circuit, the amplifier can be OP-80, R determines

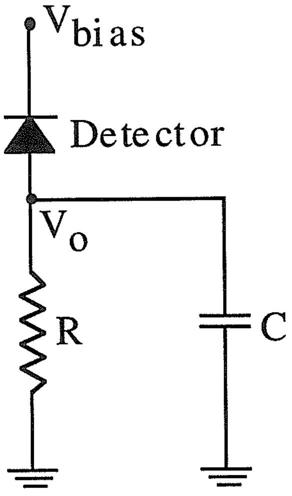

Figure B.2: Circuit with capacitor load.

the gain, and the detector bias is independent of R.

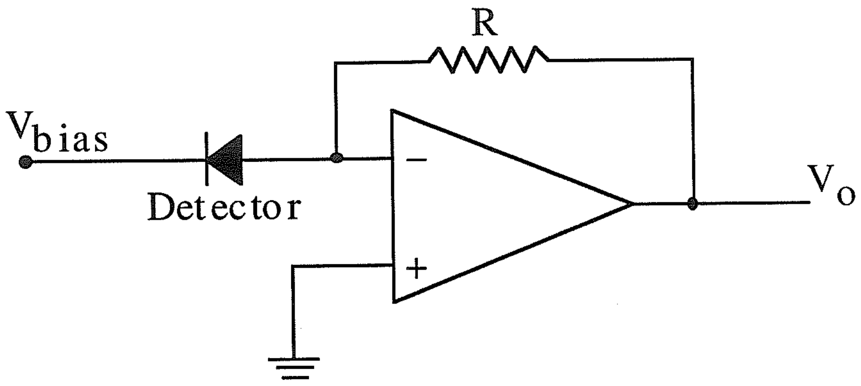

Figure B.3: Circuit used in experiments.

# References

[1] see, for example, B. F. Levine, K. K. Choi, C. G. Bethea, J. Walker, and R. J. Malik, "New 10 $\mu$m infrared detector using intersubband absorption in resonant tunneling GaAlAs superlattices," Appl. Phys. Lett., vol. 50, no. 16, pp. 1092-1094, 1987.